

Article

A Parametric Approach for Conceptual Integration and Performance Studies of Liquid Hydrogen Short–Medium Range Aircraft

Vittorio Cipolla ^{1,*}, Davide Zanetti ², Karim Abu Salem ¹, Vincenzo Binante ² and Giuseppe Palaia ¹

¹ Department of Civil and Industrial Engineering, University of Pisa, Via G. Caruso 8, 56122 Pisa, Italy; karim.abusalem@ing.unipi.it (K.A.S.); giuseppe.palaia@phd.unipi.it (G.P.)

² SkyBox Engineering, Via G. Caruso 8, 56122 Pisa, Italy; d.zanetti@skyboxeng.com (D.Z.); v.binante@skyboxeng.com (V.B.)

* Correspondence: vittorio.cipolla@unipi.it

Abstract: The present paper deals with the investigation, at conceptual level, of the performance of short–medium-range aircraft with hydrogen propulsion. The attention is focused on the relationship between figures of merit related to transport capability, such as passenger capacity and flight range, and the parameters which drive the design of liquid hydrogen tanks and their integration with a given aircraft geometry. The reference aircraft chosen for such purpose is a box-wing short–medium-range airplane, the object of study within a previous European research project called PARSIFAL, capable of cutting the fuel consumption per passenger-kilometre up to 22%. By adopting a retrofitting approach, non-integral pressure vessels are sized to fit into the fuselage of the reference aircraft, under the assumption that the main aerodynamic, flight mechanic, and structural characteristics are not affected. A parametric model is introduced to generate a wide variety of fuselage-tank cross-section layouts, from a single tank with the maximum diameter compatible with a catwalk corridor to multiple tanks located in the cargo deck, and an assessment workflow is implemented to perform the structural sizing of the tanks and analyse their thermodynamic behaviour during the mission. This latter is simulated with a time-marching approach that couples the fuel request from engines with the thermodynamics of the hydrogen in the tanks, which is constantly subject to evaporation and, depending on the internal pressure, vented-out in gas form. Each model is presented in detail in the paper and results are provided through sensitivity analyses to both the technologic parameters of the tanks and the geometric parameters influencing their integration. The guidelines resulting from the analyses indicate that light materials, such as the aluminium alloy AA2219 for tanks' structures and polystyrene foam for the insulation, should be selected. Preferred values are also indicated for the aspect ratios of the vessel components, i.e., central tube and endcaps, as well as suggestions for the integration layout to be adopted depending on the desired trade-off between passenger capacity, as for the case of multiple tanks in the cargo deck, and achievable flight ranges, as for the single tank in the section.

Keywords: hydrogen propulsion; aircraft design; conceptual integration; performance assessment



Citation: Cipolla, V.; Zanetti, D.; Abu Salem, K.; Binante, V.; Palaia, G. A Parametric Approach for Conceptual Integration and Performance Studies of Liquid Hydrogen Short–Medium Range Aircraft. *Appl. Sci.* **2022**, *12*, 6857. <https://doi.org/10.3390/app12146857>

Academic Editor: Florian Linke

Received: 22 June 2022

Accepted: 2 July 2022

Published: 6 July 2022

Publisher's Note: MDPI stays neutral with regard to jurisdictional claims in published maps and institutional affiliations.



Copyright: © 2022 by the authors. Licensee MDPI, Basel, Switzerland. This article is an open access article distributed under the terms and conditions of the Creative Commons Attribution (CC BY) license (<https://creativecommons.org/licenses/by/4.0/>).

1. Introduction

According to ACARE ([1]) and European Commission ([2]), the main milestones of the path towards sustainable aviation are a significant reduction in CO₂ (–75%) and NO_x (–90%) emissions by 2035, and the total decarbonisation within 2050. To achieve these goals, the second one in particular, the synergy between two or more of the following enabling technologies would be needed: ultra-efficient airframes, full or hybrid–electric propulsion, and sustainable drop-in or non-drop-in fuel, as, for example, hydrogen. The low energy density of batteries makes electric propulsion suitable for aircraft up to the regional category, whereas drop-in and non-drop-in fuel may be adopted in Short-to-Medium Range (SMR)

aircraft, in particular those meeting the ICAO Aerodrome Reference Code element 2 “C” (e.g., Airbus 320, Boeing 737, etc.). Adopting hydrogen as fuel is among the promising ways to achieve the decarbonisation goal ([3–5]), since it has very high energy density and its combustion does not produce CO₂. On the other hand, embarking gaseous hydrogen is not feasible, since it would require tanks about 3000 times larger than current ones; therefore, hydrogen needs to be stored in liquid conditions by means of a proper combination of cryogenic temperature and high pressure.

From the decarbonisation point of view, hydrogen is to be considered more as an energy storage than as fuel since there are no direct natural sources on Earth. The hydrogen can be obtained by processing various sources, such as hydrocarbons, biomass, and water. These processes have their own CO₂ emission levels, which should be considered in the total emissions balance. However, this estimation is dependent on the energetic policy and infrastructure of the nation in which the aircraft is operated; moreover, although hydrogen combustion does not release CO₂, it generates water and NO_x, whose effects on climate change are under study. Another important point about the application of this technology is the impact on airport infrastructure, as well as the choice of generating hydrogen on-site or not. For the reasons above, an estimation of the direct and non-direct emission is omitted in this paper, which should be regarded as a feasibility study of the application of the hydrogen propulsion technology to aircraft.

The storage system for liquid hydrogen, hereafter indicated as LH₂, is thus made of large tanks with appropriate thermal insulation, whose integration with the aircraft raises questions about the effective achievable benefits under given operational constraints, as, for example, the minimum number of passengers and flight range. This aspect opens to new research opportunities which touches the aforementioned ultra-efficient airframes, i.e., aircraft architectures, different than the conventional tube-and-wing one, that can boost the adoption of new technologies leveraging on their higher aerodynamic efficiency. In fact, since the conventional tube-and-wing architectures are mature and modifying the geometries of fuselage or wings would move the design far from the current optimal solutions, considering different architectures can facilitate the introduction of LH₂ propulsion technologies from the very early stages of the design.

A previous example of addressing a similar research question is given by the European project PARSIFAL ([6–9]), in which a box-wing aircraft designed for the SMR category (Figure 1a) has been assessed under the operational and environmental standpoints.

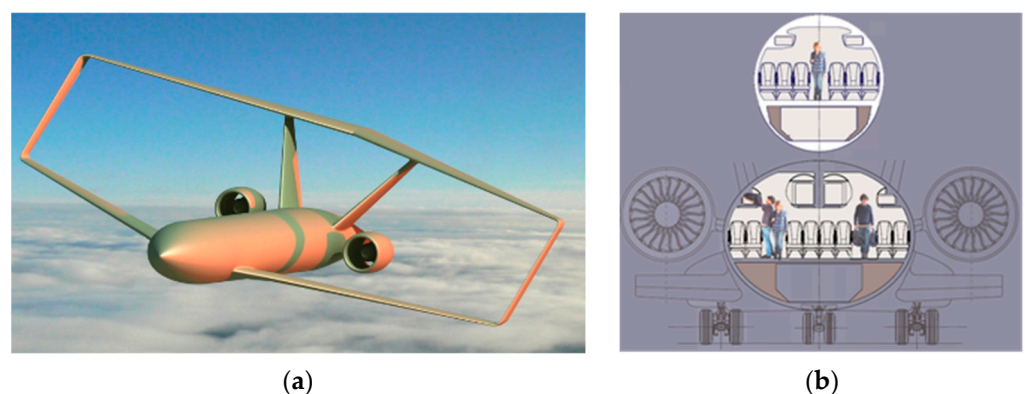


Figure 1. PARSIFAL project: (a) artistic representation of the box-wing aircraft object of study; (b) comparison between cabin cross-sections for conventional (top) and PARSIFAL cases (bottom).

Assuming adoption of conventional turbofan engines, results have shown a potential of reducing fuel burnt by 22% per seat-kilometres, with an impact on both CO₂ and non-CO₂ emissions, hence on short-term and long-term global warming and temperature change potential ([10]). The box-wing aircraft investigated in PARSIFAL is the result of a design strategy that exploits the superior aerodynamic performance of the box-wing, known since the first studies carried out by L. Prandtl in the early 1920s ([11]). In PARSIFAL,

the higher span efficiency of the box-wing is exploited to significantly increase the number of passengers while keeping the wingspan below 36 m; thus, placing the aircraft in the same segment of the aircraft compliant with the ICAO Aerodrome Reference Code element 2 “C”. This competitive advantage is obtained by designing a larger fuselage, with a double aisle and 8-seats abreast cabin, which increases the maximum number of passengers from less than 190 to more than 300 (see Table 1 for details).

Table 1. Main characteristics of the box-wing aircraft studied in the project PARSIFAL.

Parameter	Box-Wing Aircraft
Aircraft overall length	44.32 m
Aircraft overall height	9.43 m
Fuselage internal height (max.)	4.05 m
Fuselage internal width (max.)	5.40 m
Fuselage cross-section aspect ratio (height/width)	0.75
Cabin layout	Double aisle, 2-4-2 abreast
Seat pitch	0.744 m
Maximum seat capacity	308

Can this increase in the internal volume facilitate the integration of LH₂ tanks, without significant penalisation of transport capabilities? The present paper aims to assess the potential given by the synergy between the LH₂ propulsion and the box-wing architecture by means of a retrofitting approach. This means that the box-wing aircraft described in Table 1, and more in detail in Section 2.6.1, is modified at a conceptual level to integrate cylindrical LH₂ tanks in the fuselage and then the whole system is analysed to define the overall aircraft performance. The retrofitting approach does not bring optimal solutions since it does not allow to modify the external shape of the aircraft, but it allows to obtain results relying on well-studied aerodynamics, flight mechanics, and structural characteristics ([8,12]), which—at least for this conceptual level of investigation—can be considered as not affected by the tank integration. Among the hypothesis concerning flight mechanics, it is assumed that the Static Stability Margin varies within the interval estimated for the reference aircraft.

The paper is organised as follows: Section 1 introduces the scope of this work and state of the art about studies dealing with the design of aircraft with LH₂ propulsion; Section 2 provides both an overview of the retrofitting approach adopted for the analysis and details about the implemented models, focusing on geometric, structural, and thermodynamic ones; Section 3 presents the results of sensitivity analyses carried out against the design parameters recognised as most relevant; Section 4 summarises the main outcomes and indicates some possible paths to improve the research. Finally, an Appendix provides supplementary information about the discussed topics.

1.1. Scope of the Work

The scope of this work is to identify of the most significant design parameters governing the design of LH₂ tanks and their integration within the aircraft, considering only the volumes available inside the fuselage, in order to avoid any variation in the shape of the reference aircraft. In order to implement standard methods for structural design and thermodynamic analysis, non-integral metallic tanks are considered assuming the typical shapes of pressure vessels. Different solutions based on integral tanks and/or composite materials are not considered because of the limitations of the structural model adopted here.

Tanks–fuselage integration is then parametrised through a set of variables which affect tanks geometry, structural behaviour, and thermodynamic performance. Time-marching simulations are then performed considering the thermodynamic conditions of hydrogen, which is stored in cryogenic conditions and thermally insulated with a passive system, such as one or more insulant layers covering the whole internal or external tank surface. This

implies that the LH₂ is subject to a continuous heat exchange with the external environment, which causes an evaporation process resulting in an increase in the internal pressure. When this latter reaches a preassigned value, said venting pressure, gaseous hydrogen is vented-out to avoid internal pressure increase. Moreover, venting stops only if the flow of LH₂ towards the engines is strong enough to determine a net reduction in the internal pressure. This introduces an additional mechanism leading to LH₂ depletion, which can be properly evaluated only by coupling the mission simulation with the thermodynamic analyses.

1.2. State of the Art

Studies on the use of hydrogen for the aircraft propulsion started around 1950, inside programs aimed at the introduction of new fuels to extend the range and ceiling of military spy planes, trying to avoid combustion shortcomings of traditional JP fuels at high altitudes. One of these projects is the NACA “Project Bee” ([13]), which developed a notable series of reports around 1956 ([14–17]). Later, in the 1970s, in response to oil crises, NASA commissioned studies for the replacement of conventional aviation fuel: the candidates were hydrogen and methane. The main U.S. aircraft manufacturers proposed a wide range of aircraft designs, ranging from short-haul to intercontinental jets ([18–20]), along with airport integration feasibility studies ([21]) and plans for development programs. In 1988, a USSR project developed the TU-155 testbed, which used hydrogen and other gasses for the turbojet feeding.

In more recent years, the European Union gave a new motivation to the research about hydrogen as an energy vector, setting up dedicated research programs, such as CRYOPLANE ([22]) and CHATT ([23]). The aim of these studies is the decarbonisation of the transport industry, the development of a more sustainable energetic market, and an improvement in the EU energetic independence ([1,2]).

Concerning the aircraft design perspective, reference works are [18–20,24,25] and [26]. In such studies, the influence of the hydrogen storage state, engine technology, and tank–aircraft configuration integration are studied. Specific information about engines can be found in [15,17,27,28], with different engine architecture options aiming to enhance performance or to minimise the changes from current technology. Tank design is studied in [14,16,25,29–32], where the problems of the insulation, structural design, and thermodynamic state simulation are addressed. The level of detail of the aforementioned studies is summarised in Table 2.

Table 2. Level of detail of most relevant studies reported in state-of-the-art analyses.

Study	Field of Study	Level of Detail
[17–20,24,25]	Aircraft design	Conceptual, aircraft level
[26]	Aircraft design	Conceptual, aircraft and systems level
[15,28]	Engine	Experimental
[27]	Engine	Conceptual
[14]	Tank	Experimental
[16,31,32]	Tank	Conceptual
[29]	Tank	Conceptual and FEM analysis

2. Overall Analysis Approach and Implemented Methods

2.1. Data and Assumptions on LH₂ Technology

As reported in [18–20,22,24–26,30,32], LH₂ propulsion technology brings significant changes in aircraft design; they mainly concern the turbofan engines and the LH₂ storage, as shown in the following paragraphs.

2.1.1. LH₂ Turbofan Engines

The use of H₂ as fuel in the combustion chamber of a turbomachinery has been studied in [17,19,22,25,27,28]. The combustion of H₂ is possible in a wider range of pressures and fuel/air mixtures than those allowed by JP4 (Figure 4 in [17]). Therefore, it is possible

to convert ordinary turbofans to run on H_2 , or design new engines for new operative conditions ([19]). In this work, the engine design has been preserved, following the “retrofit” approach proposed in [27], in order to minimise engine modifications.

Despite the marginal variation in the engine design, there is the need of a heat exchanger (HE), in order to shift the hydrogen state from storage conditions to combustion chamber injection conditions. In [22,27], some HE options have been proposed; however, in order to minimise the changes to the engine and the airframe, in this work, the HE will be considered located after the Low Pressure Turbine. For an engine with this configuration, delivering the same thrust of a JP4 fuelled engine, in [27] the authors indicate that the SFC decreases by 64.71% and Turbine Entry Temperature decreases by 31.5 K, with a significant improvement in engine life. The weight of the engine itself is the same as a conventional one, but the HE adds 1% to the overall engine weight ([27]).

2.1.2. LH_2 Storage

The most relevant change introduced by the LH_2 propulsion is the need for a new kind of tank. A hydrogen tank should guarantee thermal insulation and pressurisation in order to preserve the storage state of the hydrogen. Furthermore, in the case of tank cracks or failures, a proper level of pressurisation is needed to prevent oxygen from entering the tank, which can lead to explosive mixtures ([25,33]). The hydrogen storage state is an important point of discussion, since it influences the hydrogen density and the tank structural design; the main options are the three blue areas highlighted in Figure 2, taken from [34].

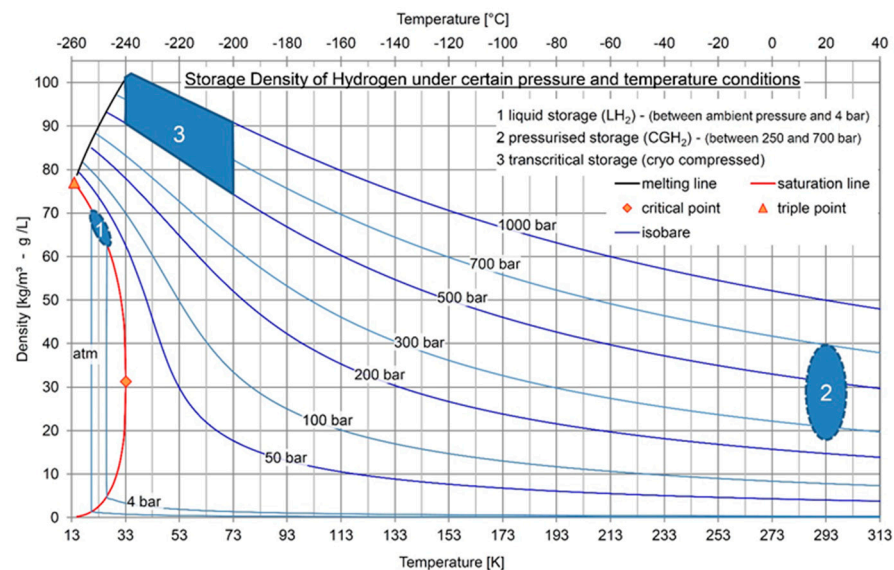


Figure 2. Storage density of hydrogen for different pressure and temperature conditions ([34]).

Most of the studies ([14,16,18–20,22,24–26,29,31,32,34,35]) concern tanks at storage states close to region 1 (see Figure 2), where the hydrogen is in a saturated liquid form (LH_2), the pressure varies between 0.1 and 0.4 MPa and temperatures are lower than 30 K. In region 3, gaseous hydrogen (H_2) is stored at a higher density (+33%) but the storage pressure is considerably higher (50–100 MPa), which leads to heavier tanks and safety issues, since the pressure rises faster under incoming heat flux [24]. Storage solutions in region 2 exhibit the lowest density, hence larger tanks which are difficult to integrate with the aircraft.

For the reasons above, in this work the hydrogen is considered stored in a state close to the region 1. In such state, both liquid and gaseous phases are present (biphasic saturated state), hence, LH_2 cannot fill the total internal volume of the tank. Liquid and gaseous saturated phases are at equilibrium and show the same temperature and the same pressure; therefore, they constitute a saturated liquid–gas mixture. In saturation state, the gas law is no more valid, and pressure and temperature of the mixture show a bijective relation

not dependent on other variables (Figure 3). For the purposes of this work, the physical properties of the two phases were taken from [36] and used in the form of lookup tables for data interpolation.

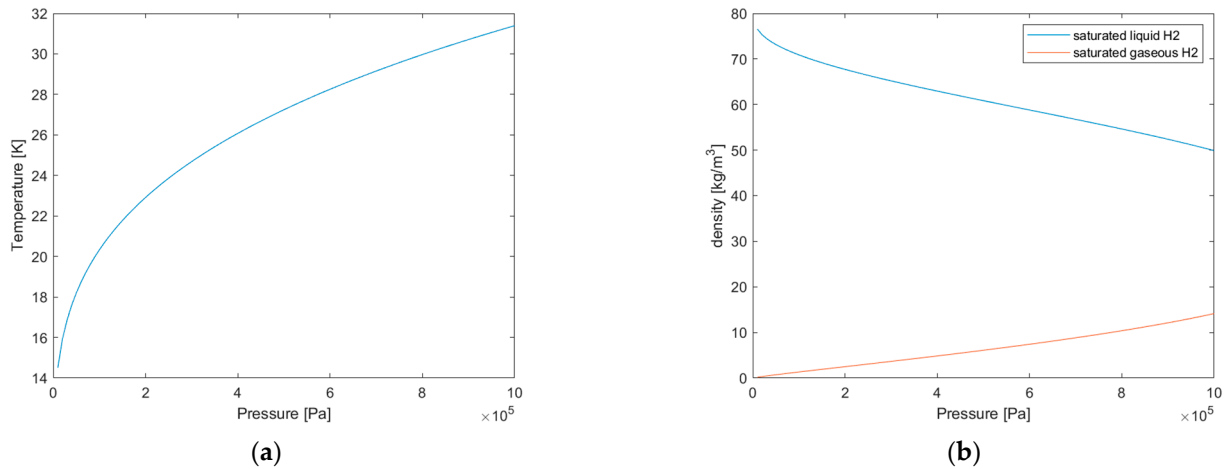


Figure 3. Temperature–pressure (a) and density–pressure (b) relations for saturated H₂.

Since the heat flux directed from the external environment towards the tank causes a pressure raise ([31]), tanks need a venting valve which avoids the internal pressure overcoming the maximum design pressure. The venting of H₂ represents a loss of fuel and leads to a reduction in the aircraft flight range; therefore, an insulation system is required to minimise the heat exchange and thus the pressure increase. For any assigned reference internal pressure, the internal volume cannot be completely filled with LH₂, because in the case of pressure rise there would not be H₂ to be vented and pressure could not be lowered. Anyway, when considering a partial filling, it must be verified that the stored LH₂ does not expand (Figure 3b) to the maximum capacity of the tank when it reaches the venting pressure. For the reasons above, the authors of [24–26] studied pressure levels and filling volumes in order to have a reasonable fuel density, while considering a minimum pressure to avoid contamination. The heat flux across the tank walls depends on three main thermal exchange stages: convection and radiation with the external environment, conduction across the tank insulant and structures, and the heat exchange inside the fluid ([24,25]).

There are different ways to guarantee the insulation of the tank; the simplest is to use a thick layer of insulating material ([14,16]), such as closed cells foams; other methods use open cell foams and a mylar liner ([24,25]) or a double-walled tank, with vacuum between the walls and multi-layer insulation on each side of the vacuum jacket, in order to prevent thermal exchange by radiation ([34]). In this work, simple closed cell insulation foams are considered. The types are a polystyrene foam, a polymethacrylimide foam, and a polyurethane foam, with the characteristics summarised in Table 3. Data regarding polystyrene foam are taken from [16], whereas data about polymethacrylimide and polyurethane foams are from [25]. Thermal conductivity data about foams are taken from [16,25] and reported in Figure 4. It can be noted that, for this kind of material, the thermal conductivity strongly depends on the temperature.

Table 3. Properties of insulant materials.

Material	ρ_i , Density [kg/m ³]	K_i , Conductivity [W/(m K)]
Polystyrene foam (PS)	25.6	0.015–0.045
Polymethacrylimide foam (PMI)	51.1	0.005–0.037
Polyurethane foam (PRU)	32.0	0.005–0.025

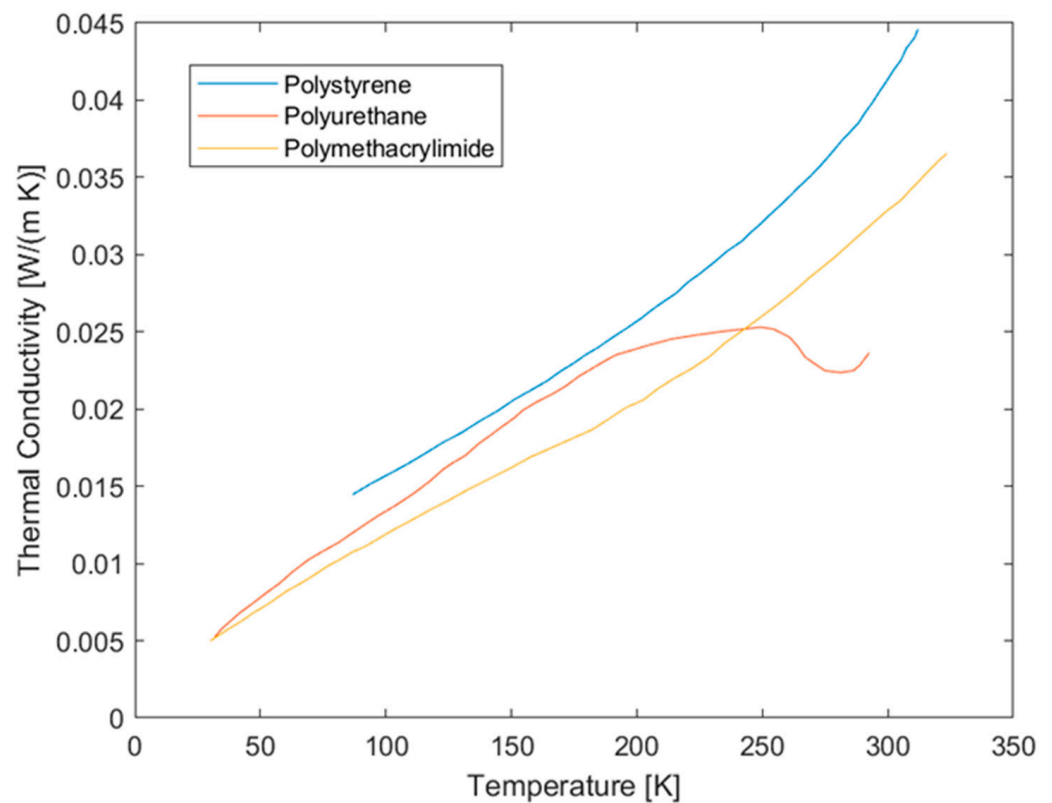


Figure 4. Thermal conductivity of insulation foams.

As in [24], in order to keep the design of aircraft-borne LH₂ tanks as general as possible and applicable to different integration solutions, non-integral tanks with inner metallic structural vessel and external foam insulation were taken into account. Since more tanks can be installed in the same fuselage portion, the thermodynamic analysis should take their mutual interaction into account. To reduce the computational time, this problem was simplified assuming that each tank is thermodynamically isolated from the others and that the foam insulation is in contact with the air flowing at the aircraft flight speed. This means that the insulation effect of the calm air inside the fuselage as well as the additional thermal resistance of the fuselage skin are neglected, leading to an overestimation of the heat exchange and providing conservative results on aircraft performance.

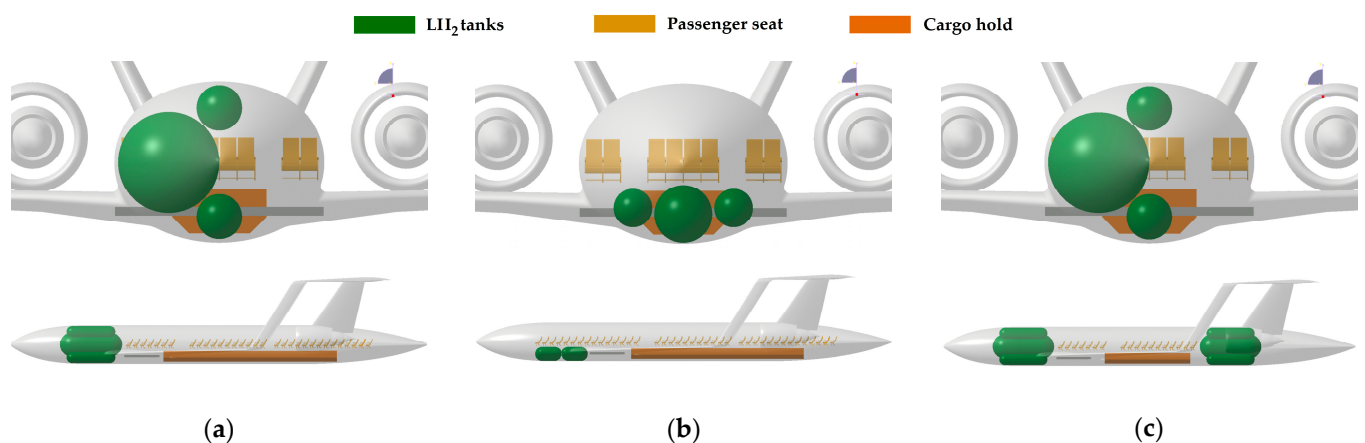
Concerning the structural materials, three metal alloys were considered: the stainless steel grade 301 (SS301), the aluminium alloy 2219 (AA2219), and the titanium alloy Ti-5Al-2.5Sn. The mechanical characteristics at cryogenic temperature conditions (20 K) were extrapolated from [37] and are here summarised in Table 4. These materials have been considered in several of the studies cited in the present section, and details are not reported for sake of conciseness.

Table 4. Properties of structural metallic materials at cryogenic conditions ($T = 20\text{ K}$), for 1.6-mm-thick sheets ([37]).

Material	Treatments	σ_y , Yielding Strength at $T = 20\text{ K}$ [MPa (10^3 psi)]	σ_u , Ultimate Tensile Strength at $T = 20\text{ K}$ [MPa (10^3 psi)]	E , Modulus of Elasticity at $T = 20\text{ K}$ [GPa (10^6 psi)]	ρ_s , Density [kg/m ³]
Stainless steel grade 301 (SS301)	Tempered (3/4 hardened)	1585 (230)	2000 (290)	207 (30)	7890
Aluminium alloy 2219 (AA2219)	Heat-treated, cold worked, then artificially aged (T8)	448 (65)	655 (95)	76 (11)	2825
Titanium alloy Ti-5Al-2.5Sn	Extra-low interstitial grade, annealed	1344 (195)	1655 (240)	124 (18)	4480

2.2. Overview of the Analysis Method

The analysis method adopted here aims at defining the relevant parameters for the integration of hydrogen tanks into the fuselage of an SMR aircraft with assigned shape and aerodynamic characteristics, previously determined considering turbofan engines propelled with kerosene. Therefore, the present method is based on the main assumption that, at a conceptual level, a LH₂ transport aircraft sharing the same external shape of a conventional Jet A fuel aircraft, can be studied modifying the characteristic of this latter, once the volume, structural mass, and insulation foam mass needed for tanks is estimated. Moreover, it is assumed that each tank is a non-integral vessel with a circular cross-section, composed of a cylindrical central tube and semi-ellipsoidal endcaps, with a structure made of unstiffened shells covered by a uniform layer of insulation foam (see Figure 7 Section 2.3). For a better understanding, an artistic representation of tank–fuselage integration layouts is given in Figure 5, which shows both solutions aiming at maximising the available internal volume while keeping continuity between fore and aft fuselage through a “catwalk” (Figure 5a,c), and solutions which limit the tanks’ impact on the fuselage design as in Figure 5b. The parametric description of all these geometries is provided in Section 2.3.

**Figure 5.** Illustration of possible tanks–fuselage integration layouts: (a) full-section with “catwalk”, (b) part-section with cargo deck occupation, (c) multiple groups of tanks (full-section case).

The analysis method is represented in Figure 6 and implemented as follows:

- The available fuselage section is approximated as an elliptic area, hence the tanks’ layout and the external radius of each of them are parameterised as functions of a single variable;

- It is assumed the insulation foam is the outermost layer of the tank, hence once its thickness is given, the external radius of each tank structure can be calculated;
- The ASME Boiler and Pressure Vessel Code ([38,39]) are then adopted to define the structural thickness of each tank, considering the load conditions defined in [26]. The structural sizing takes both the insulation foam mass and the internal volume occupied by LH₂ into account; therefore, at the end of this step the tanks' groups are fully defined in terms of geometries, masses, and internal volumes;
- The aircraft empty weight is updated and, for those cases in which tank installation causes limitations of the cabin length available for passengers, the same is completed for payload;
- Once the aircraft take-off weight is updated and the initial embarked LH₂ is known, a time-marching simulation of the flight mission is performed considering that at each time step all the non-empty tanks contribute equally to feed the engines;
- The time-marching simulation is coupled at each timestep with thermodynamic analyses that evaluates, for each tank, masses, pressures, temperatures, etc., of both liquid and gaseous hydrogen. These analyses allow to estimate the mass flow of evaporated hydrogen to be expelled in the atmosphere through the venting valve;
- By summing up the LH₂ flow going to the engines and the vented gaseous hydrogen flow, the hydrogen consumption is simulated through the following flight phases: preparation for flight (holding time between LH₂ fuelling and engine start), taxi-out, take-off run, take-off path, climb, and cruise. The mission ends once one of the following conditions is reached:
 - The total amount of LH₂ in all the tanks is lower than the fuel needed for the remaining flight phases (descent, diversion, approach, and landing) and for reserve;
 - The internal pressure of all the tanks is lower than an assigned threshold value.
- If the cruise is successfully completed, the considered tank layout is associated to a set of output data including flight range, maximum number of passengers, aircraft empty weight, burnt and vented LH₂.

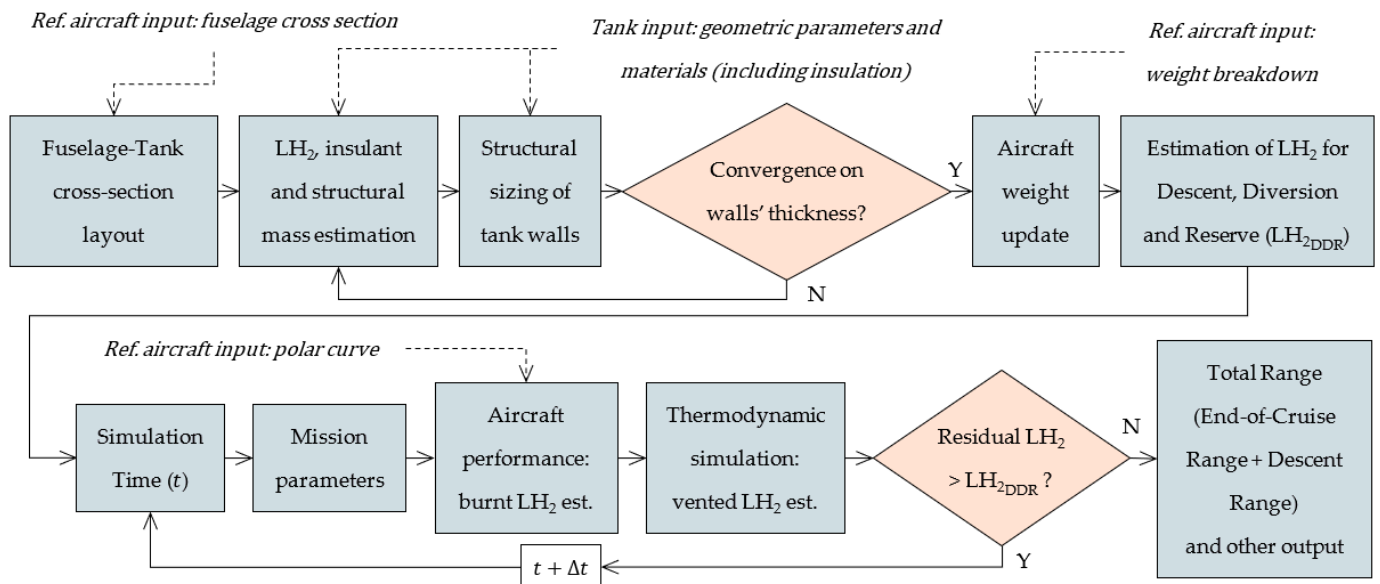


Figure 6. Scheme of the analysis method workflow.

The following paragraphs provide a detailed description of all the above-mentioned steps and their implementation in a MATLAB code with most relevant results.

2.3. Parametric Definition of Tanks Geometry

The geometry of a generic longitudinal section of any of the tanks is defined as in Figure 7, for which it assumed that the thickness of insulation foam (t_{ins}), central walls (tc), and endcap walls (te) are uniform.

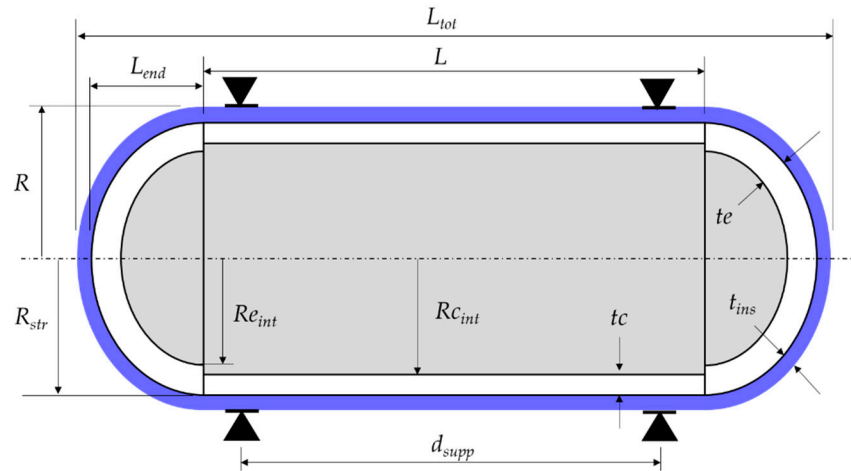


Figure 7. Longitudinal section of a generic hydrogen tank composed of a cylindrical central part and two semi-ellipsoidal endcaps, both covered by an external layer of insulation material (in blue).

The other relevant parameters indicated in Figure 7 are:

- R : external radius of the tank;
- R_{str} : external radius of the structural part, same for both central tube and endcaps;
- $R_{c_{int}}$: internal radius of the cylindrical tube;
- $R_{e_{int}}$: internal radius of endcaps measured at the junction with the cylindrical tube;
- L : length of the cylindrical tube;
- L_{end} : longitudinal dimension of the semi-ellipsoidal endcap, whose ratio versus R_{str} , also called endcaps aspect ratio and indicated as f_{end} , is given in Equation (1);

$$f_{end} = \frac{L_{end}}{R_{str}} \quad (1)$$

- L_{tot} : total length of the tank, for which the relation in Equation (2) stands:

$$L_{tot} = L + 2 \cdot R_{str} \cdot f_{end} + 2 \cdot t_{ins} \quad (2)$$

- d_{supp} : distance between supports providing the structural connection between the tank and the fuselage.

The parametric description of tanks' geometry was focused on the description of the space occupied by the tanks within the fuselage cross-section, and it was conceived to handle a high number of tank layouts using a small number of parameters. The input needed by the parametric model is the dimensions of the available fuselage section and the position of the main tank in the fuselage cross-section. These inputs can be provided in a different manner, depending on the desired layout:

- Full-section layout: a set of tanks properly sized to occupy the elliptic cross-section of the fuselage, hence reducing the space available for passengers and containers;
- Part-section layout: a set of tanks properly sized to occupy only the parts of the fuselage cross-section below and/or above an assigned height, hence not reducing the space available for passengers;

In addition, the presence of "catwalks", i.e., corridors which allow crews and passengers to walk through the portion of fuselage occupied by the LH₂ tanks, and multiple groups of tanks (both with full-section and part-section layout) can be specified.

Since space constraints are given through section borders, all the considered layouts are conceived for fuselage parts that can be approximated as cylindrical, as the central ones, whereas fore and aft fuselage volumes are not considered as available for tank integration in this study.

2.3.1. Full-Section Layout

The design concept behind a full-section layout consists of embarking large quantities of LH₂ by replacing the fuselage volume occupied by passengers and containers with fuel tanks. Such a solution has the potential advantage of allowing long-range flights, with a penalisation in terms of maximum transportable payload.

The full-section layout is defined for an elliptic fuselage internal section, whose width and height are given by the semi-major axis (w) and the semi-minor axis (h), respectively. These parameters also determine the aspect ratio f , according to Equation (3).

$$f = \frac{h}{w} \quad (3)$$

Normalising the semi-major axis ($w = 1$), the following analytical treatment can refer to non-dimensional variables.

The space available for the main tank (or “Tank 0”) is defined as the biggest circle (C₀) inscribed in the ellipse, fulfilling the condition of tangency in the point $T_0 \equiv (\cos t_0, f \cdot \sin t_0)$, where t_0 is the arbitrary chosen polar coordinate indicated in Figure 8a. The picture provides the graphical representation of C₀, showing its symmetry to the horizontal axis. The centre of C₀ has coordinates $C_0 \equiv (x_0, y_0)$ given by Equation (4), whereas the radius r_0 is given by Equation (5).

$$C_0 : \begin{cases} x_0 = \cos t_0 \cdot (1 - f^2) \\ y_0 = 0 \end{cases} \quad (4)$$

$$r_0 = f \sqrt{f^2 \cdot \cos^2 t_0 + \sin^2 t_0} \quad (5)$$

The space available for side tanks, “Tank 1” and “Tank 2”, is then defined setting the conditions that describe the circles C₁ and C₂, respectively, at left and right of C₀ as Figure 8b shows. As Equations (6)–(9) show, once C₀ is known, C₁ and C₂ centres and radii can be defined univocally.

$$C_1 : \begin{cases} x_1 = \min\left(\frac{x_0 - r_0 - 1}{2}, f^2 - 1\right) \\ y_1 = 0 \end{cases} \quad (6)$$

$$r_1 = \min\left(\frac{x_0 - r_0 + 1}{2}, f^2\right) \quad (7)$$

$$C_2 : \begin{cases} x_2 = \max\left(\frac{x_0 + r_0 + 1}{2}, 1 - f^2\right) \\ y_2 = 0 \end{cases} \quad (8)$$

$$r_2 = \min\left(\frac{1 - x_0 - r_0}{2}, f^2\right) \quad (9)$$

The following two steps consist of defining the space available for two additional couples of tanks (“Tanks 3” and “Tanks 4”) through the construction of the circles C₃ (Figure 8c) and C₄ (Figure 8d), which are tangent to the ellipse and to C₀ as well as to C₁, if in the case of C₃, or C₂, if in the case of C₄.

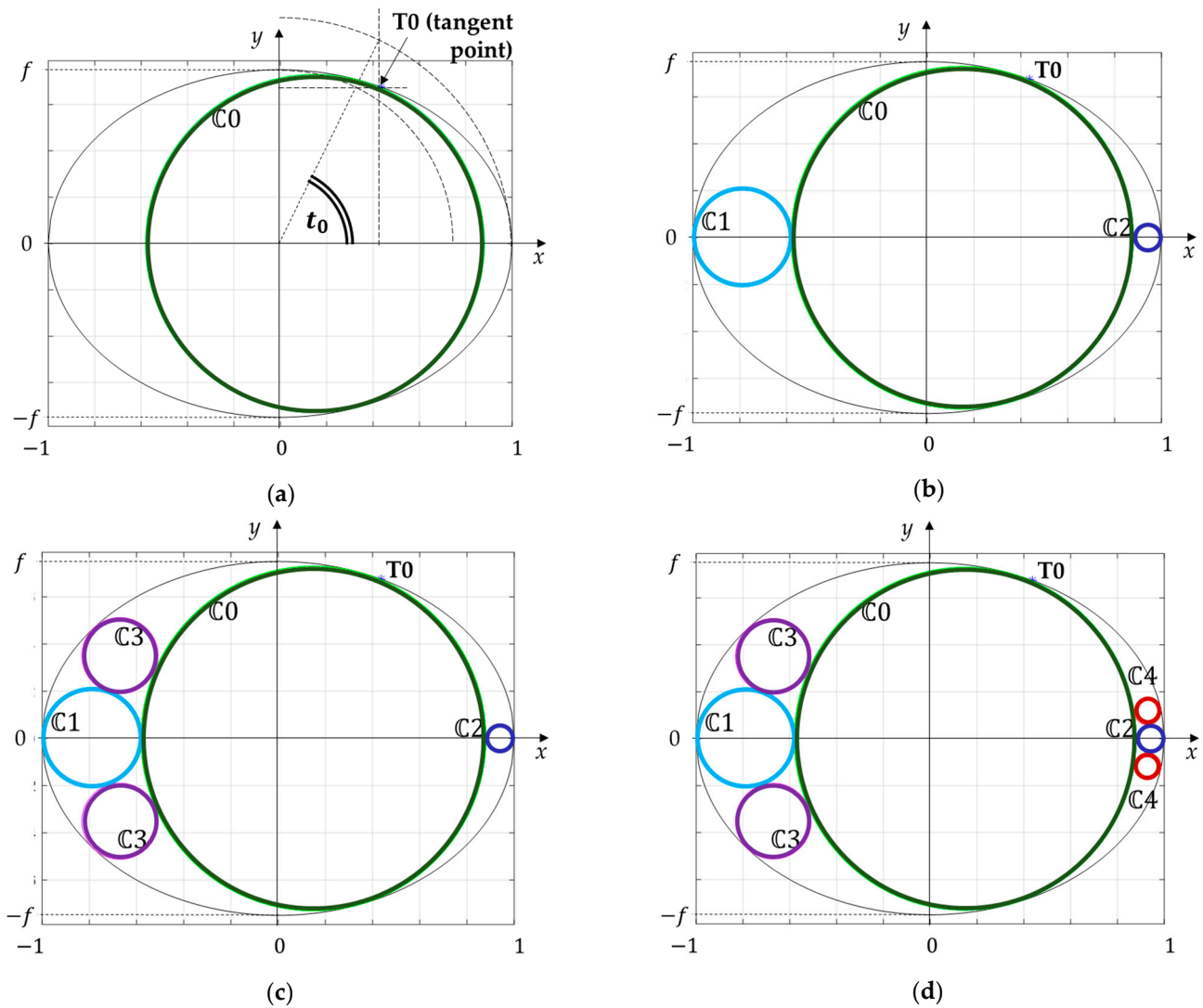


Figure 8. Full-section layout: steps for definition of the space available for the tanks within the fuselage cross-section: (a) definition of the main tank cross-section, (b) introduction of mid-size side tanks, (c) introduction of an additional couple of tanks on the left-side, (d) introduction of an additional couple of tanks on the right-side.

Considering the C3 circle belonging to the upper semi-plane, its centre $C_3 \equiv (x_3, y_3)$ and radius r_3 can be found by solving the system given by Equation (10), in which the first line introduces the condition of tangency of C3 to both C0 and C1 as a constraint for r_3 , the second line constrains the centre C3 to belong to the line perpendicular to the ellipse in an unknown point defined by the polar coordinate t_3 , and the third line sets the tangency of C3 to the ellipse through an additional constraint for r_3 . Equation (10) was solved numerically using the MATLAB *vpasolve* function and an analogous system was solved to determine C4 centre and radius.

$$\begin{cases} r_3 = \sqrt{(x_3 - x_0)^2 + (y_3 - y_0)^2} - r_0 = \sqrt{(x_3 - x_1)^2 + (y_3 - y_1)^2} - r_1 \\ \sin t_3 \cdot (x_3 - \cos t_3) - f \cdot \cos t_3 \cdot (y_3 - f \cdot \sin t_3) = 0 \\ \sqrt{(x_3 - x_0)^2 + (y_3 - y_0)^2} - r_0 = \sqrt{(x_3 - \cos t_3)^2 + (x_3 - f \cdot \sin t_3)^2} \end{cases} \quad (10)$$

The procedure here described constitutes an algorithm which allows to define the layout of a large number of tanks by varying just one parameter, t_0 , in the range $[0, \pi]$. The choice of limiting the maximum number of tanks to 7 was set for practical reasons, both

related to the technological limitations in manufacturing and using vessels with small radii, and to the computation time of the coupled mission–thermodynamic simulation, which is almost proportional to the number of tanks.

By implementing this algorithm in a MATLAB code, some geometric performance analyses were carried out varying the t_0 parameter, in order to assess the capability of covering the available area while limiting the external perimeter, since it affects the heat exchange between the LH₂ at cryogenic temperature and the external atmosphere. For this purpose, two geometric performance indicators were defined: e_a , the fraction of area covered by all the circles (A_{TOT}) defined with respect to the ellipse area as shown in Equation (11), and e_p , the normalised area–perimeter ratio defined as in Equation (12), where the denominator is A/p^2 for the circle, i.e., the maximum achievable value for a plane figure.

$$e_a = \frac{A_{TOT}}{\pi f} \tag{11}$$

$$e_p = \frac{A_{TOT}/p_{TOT}^2}{1/(4\pi)} \tag{12}$$

Figure 9 shows the results of e_a and e_p calculated for $f = 0.75$ and various t_0 values, both for the ideal case of no constraints to the minimum external radius R (a) and for the case in which the minimum value was set to 10% of the fuselage half-width (b). Figure 10 provides some examples of cross-sections to better visualise the configurations.

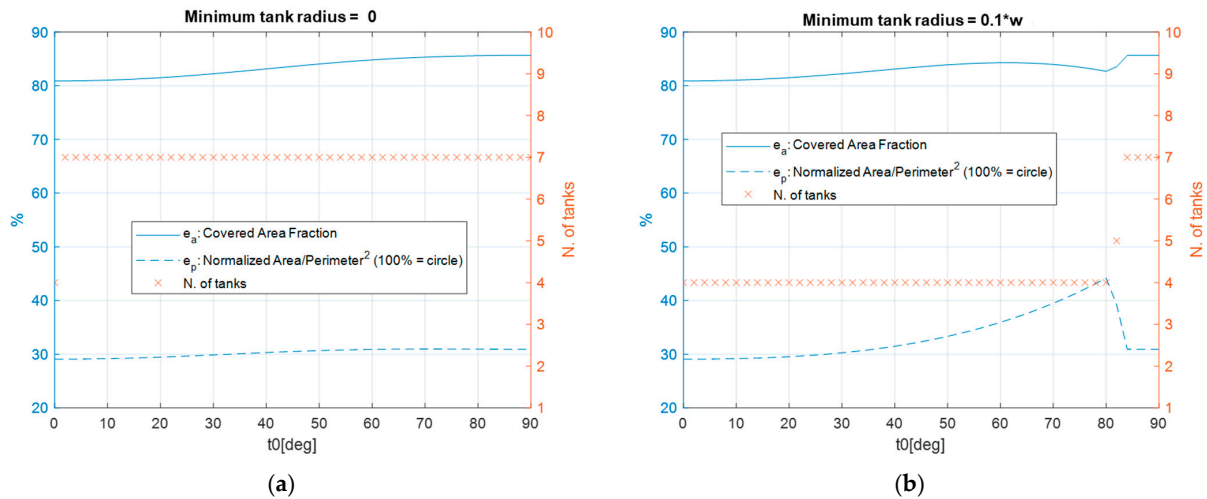


Figure 9. Geometric performance of full-section layout for $f = 0.75$ and various t_0 values: (a) no constraints on minimum radius values, (b) minimum radius set to 10% of fuselage half-width.

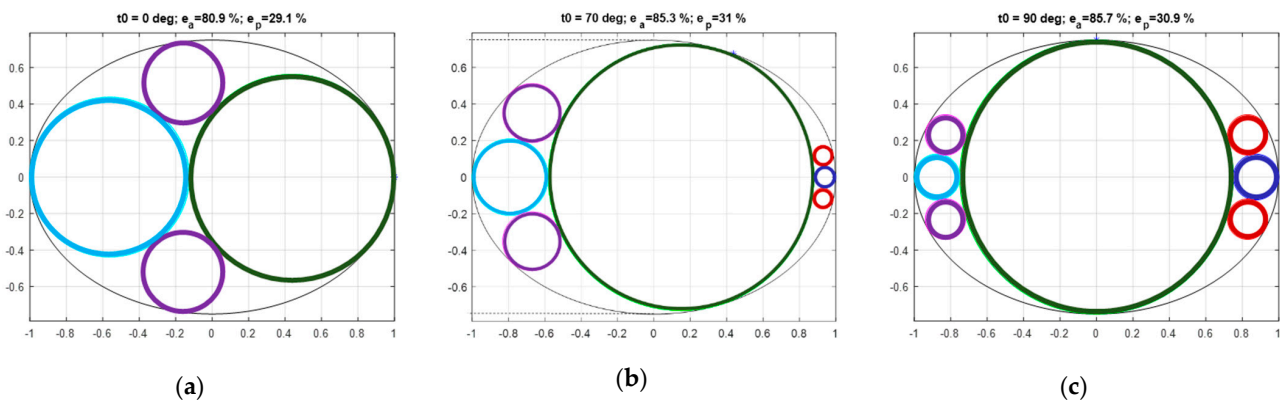


Figure 10. Examples of full-section layouts without minimum radius constraints for three different t_0 values: (a) 0° , (b) 70° , (c) 90° .

Whereas in Figure 9a each configuration with $t_0 \neq 0$ is composed of 7 tanks (see Figure 11), the minimum radius constraint reduces this number to 4 for a significant part of t_0 range. Understandably, further increasing the radius threshold extends the reduced tanks region and can bring to configurations with only 1 or 2 tanks.

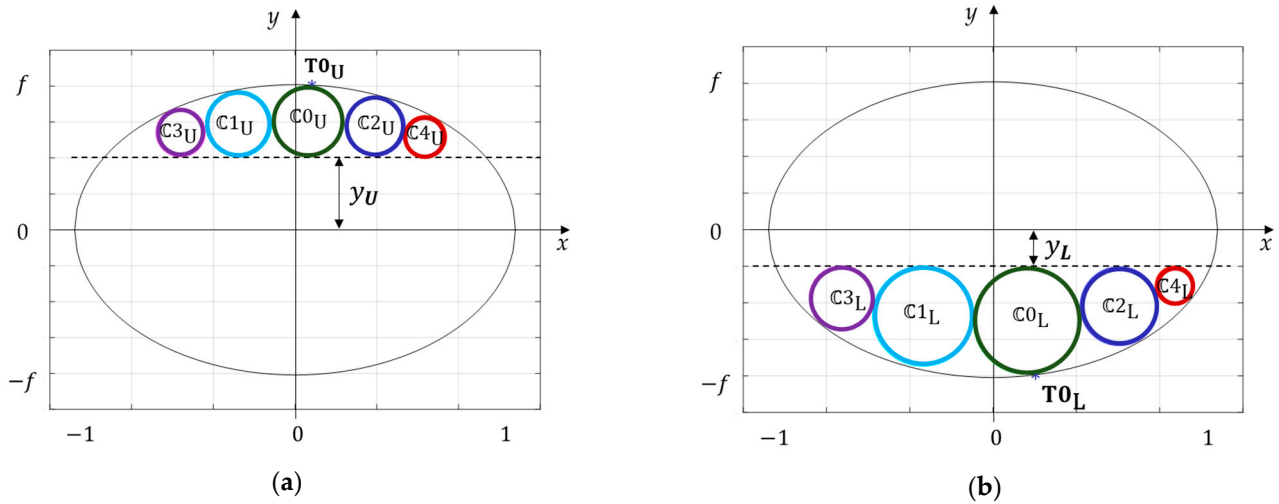


Figure 11. Part-section layouts: (a) available space in the upper part of the cross-section; (b) available space in the lower part of the cross-section.

Considering the trends shown in Figure 9, the main remarks concern:

- The low sensitivity of e_a to t_0 , for which the best solution is given by the case at $t_0 = 90^\circ$ ($e_a = 85.7\%$) but lower angles show a small reduction in e_a hence still providing a good area coverage (see Figure 12a for an example);
- The previous observation is valid both with and without the minimum radius constraint;
- e_p is quite insensitive to t_0 if the minimum radius constraint is not applied;
- The suppression of small tanks due to the minimum radius constraint causes better values of e_p .

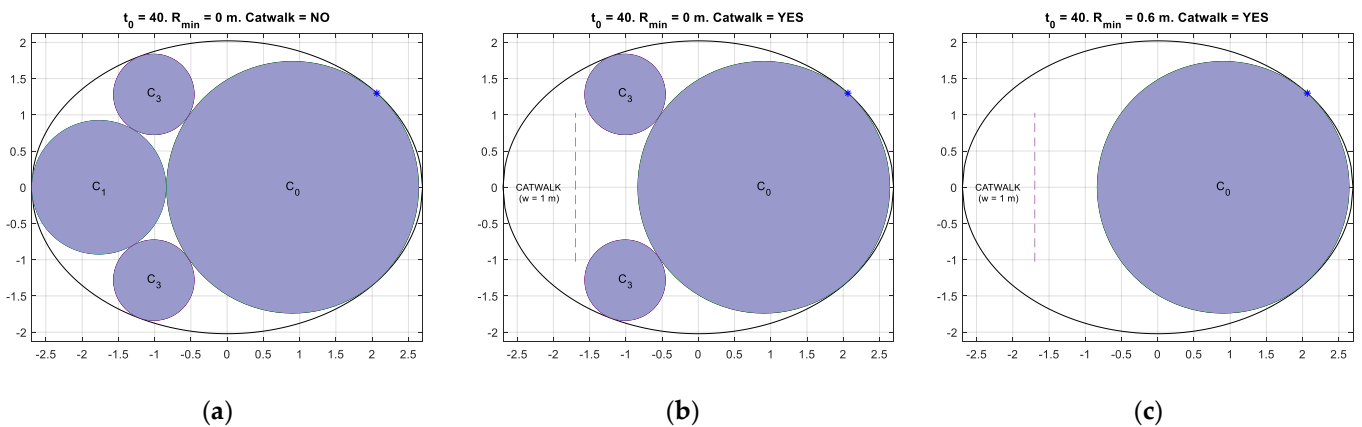


Figure 12. Examples of full-section layout for $t_0 = 40^\circ$: (a) without catwalk ($e_a = 83\%$; $e_p = 31\%$), (b) with catwalk ($e_a = 67\%$; $e_p = 45\%$), (c) with catwalk and minimum radius constraint ($e_a = 56\%$; $e_p = 100\%$).

2.3.2. Part-Section Layout

Part-section layouts are defined with algorithms similar to the full-section one by adding upper and/or lower constraints along the y direction to the available space and removing the symmetry conditions with respect to the horizontal axis.

Figure 11 shows the two possible options in which tanks are installed in the upper part of the fuselage (a), for cases in which the space above the cabin might be sufficient for tank installation, or in the lower part of the fuselage (b), which represents the case in which the lower deck is used for LH₂ storage with a partial or total reduction in the volume assigned to containers. It is worth mentioning that these layouts have the possible advantage of avoiding the reduction in cabin space, hence number of transported passengers, but at the same time can embark smaller LH₂ quantities, hence shorter flyable ranges, if compared to full-section solutions.

In the case depicted in Figure 11a, where the available space is designated through the constraint $y \geq y_U$, up to 5 circles can be constructed starting from the circle C_{0U} which depends on the tangent point belonging to the ellipse T_{0U} , whose position can be defined using the polar coordinate t_{0U} which is analogous the full-section parameter t_0 . Then, C_{0U} radius (r_{0U}) and centre $C_{0U} \equiv (x_{0U}, y_{0U})$ can be defined using Equations (13) and (14).

$$C_{0U} : \begin{cases} x_{0U} = \cos t_{0U} + f \cdot \cot t_{0U} \cdot (y_{0U} - f \cdot \sin t_{0U}) \\ y_{0U} = \frac{y_U + f \cdot \sin t_{0U} \sqrt{(f \cdot \cot t_{0U})^2 + 1}}{1 + \sqrt{(f \cdot \cot t_{0U})^2 + 1}} \end{cases} \quad (13)$$

$$r_{0U} = \sqrt{(x_{0U} - \cos t_{0U})^2 + (y_{0U} - f \cdot \sin t_{0U})^2} \quad (14)$$

Once C_{0U} is known, C_{1U} and C_{2U} are the defined setting of the tangent conditions to the ellipse, the line $y = y_U$ and to C_{0U} . The same procedure is then performed to define C_{3U} and C_{4U} , using the tangent condition to C_{1U} and C_{2U} , respectively. As an example, Equation (15) shows the system used for the construction of C_{1U} , whose solution was found numerically using MATLAB *vpasolve* function. As in Equations (13) and (14), the first two lines set the tangency to the ellipse and to the line $y = y_U$, the third equation sets the tangency to C_{0U} , and the fourth line specifies on which side of C_{0U} this condition has to be obtained. Similar systems of equations can be written to define the remaining circles.

$$\begin{cases} x_{1U} = \cos t_{1U} + f \cdot \cot t_{1U} \cdot (y_{1U} - f \cdot \sin t_{1U}) \\ y_{1U} = \frac{y_U + f \cdot \sin t_{1U} \sqrt{(f \cdot \cot t_{1U})^2 + 1}}{1 + \sqrt{(f \cdot \cot t_{1U})^2 + 1}} \\ \sqrt{(x_{1U} - x_{0U})^2 + (y_{1U} - y_{0U})^2} - r_{0U} = \sqrt{(x_{1U} - \cos t_{1U})^2 + (y_{1U} - f \cdot \sin t_{1U})^2} \\ t_{1U} > t_{0U} \end{cases} \quad (15)$$

For the case given in Figure 11b, i.e., considering as constraint $y \leq y_L$, the procedure for defining the circles is analogous to the one here presented.

2.3.3. Presence of Catwalk

The presence of a catwalk is needed to avoid physical separation between pilots' cabin and any part of passenger decks. This option was implemented only for the full-section layout since it is the only case for which the installation of tanks generates a physical barrier.

The catwalk option has the effect of suppressing only the circle C_1 (or C_2), in order to leave enough space for a side corridor and limiting the reduction in area occupied by the main circle C_0 . The algorithm is conceived to suppress C_1 (or C_2) only after the definition of the C_3 (or C_4) couple, in order to use as much as possible of the available section area. As shown in Figure 12, the possibility to use the space assigned to C_3 circles, when compatible with minimum radius constraints, allows to partially compensate for the loss of available area due to the introduction of the catwalk.

2.3.4. Multiple Groups of Tanks

The possibility to define more than one group of tanks was implemented in order to simulate the case in which the LH₂ tanks are installed in distinct fuselage compartments with the aim of providing a better mass balance and centre of gravity management. The

comparisons were performed under the constraint of keeping the total LH₂ embarked mass unvaried, which is obtained by adapting the length of the central tube of the derived tanks (\hat{L}) according to the approximated relation given by Equation (16), where n_{tg} is the number of tank groups.

$$\frac{\hat{L}}{D_{str}} = \frac{L}{n_{tg} \cdot D_{str}} - \frac{2}{3} \cdot \frac{n_{tg} - 1}{n_{tg}} \cdot f_{end} \quad (16)$$

The study of the impact of LH₂ tanks on longitudinal equilibrium and stability is out of the scope of the present paper; therefore, this option was introduced only for assessing benefits and drawbacks of dividing the same quantity of embarked LH₂ between more identical tank groups. This option can be used for both full-section and part-section layouts and with any combination of catwalk presence and minimum radius.

2.4. Structural Sizing

The structural sizing of a generic non-integral unstiffened tank is performed combining the approach described by [26], based on Federal Aviation Regulation (FAR) Part-25 ([40]), and the ASME Boiler and Pressure Vessel Code [38]. According to this latter, the allowable tensile stress of the material (σ_{all}) can be calculated as in Equation (17), in which σ_y is the yielding strength and σ_u is the ultimate strength of the material, both depending on the operating temperature T .

$$\sigma_{all} = \min \left[\frac{\sigma_y(T)}{1.5}; \frac{\sigma_u(T)}{3.5} \right] \quad (17)$$

Since Equation (17) frames the structural design in the elastic stress–strain interval, only limit conditions prescribed by FAR Part-25 were considered. They are:

- Difference between internal pressure and external pressure at limit condition (Δp) calculated as in Equation (18):

$$\Delta p = (k_{vent} \cdot p_{int} - p_{cr}) \cdot RF \quad (18)$$

where:

- p_{int} is the vessel internal pressure, whose reference value is set to 144.8 kPa (21 psi) according to the general conclusions drawn in [26];
- k_{vent} is the ratio between the venting pressure (p_{vent}), i.e., the maximum value that internal pressure reaches during normal operations, and p_{int} . According to [26], a typical value of k_{vent} is 1.1;
- p_{cr} is the atmospheric pressure at cruise, calculated using the ICAO International Standard Air model for the desired cruise altitude;
- RF is the relief valve tolerance, set to 1.1 according to FAR Part-25 and also adopted in [26].
- Inertial loads due to flight manoeuvres or gusts at the following (not combined) limit load factors, derived dividing by 1.5 the ultimate values prescribed by FAR Part-25:
 - Equal to 3 in the radial direction (n_r), referred to the most critical case for loads acting in the cross-section plane, i.e., downward loads (ultimate $n_z = +4.5$);
 - Equal to 6 in the axial direction (n_x).

Thermal loads were not considered, since it is assumed the whole metallic structure of the tank, being thermally isolated from the external atmosphere by the insulating layer, is at a constant temperature, hence there are no gradients causing additional stress. In addition, it is assumed that the supporting frames are designed to allow the thermal contraction of the tank structure, which avoids the local introduction of additional loads.

The structural design is then implemented through the following procedure:

- Given the insulation material thickness (t_{ins}) as an input, the internal radius of the central part of the vessel ($R_{C_{int}}$) is initialised with the external radius value $R_{str} = R - t_{ins}$ (see Figure 7);

- The thickness of the vessel cylindrical part (tc) is calculated considering welded joints, longitudinal or circumferential, as the most critical areas in which the static strength needs to be verified; therefore, both longitudinal and hoop stresses are calculated and compared to admissible values of the given material and type of joint. The adopted formulas are given in Equation (19), where the first and second expressions provide the thickness resulting from a design for circumferential and longitudinal stress, respectively, whereas the third term is the minimum thickness imposed by [39]. In Equation (19), η_w is the welding efficiency as defined in [38], which for butt joints is set to 1 if full radiographic examinations are carried out, 0.85 in the case of spot examinations, and 0.7 otherwise. For the present study, a prudential value of 0.85 was chosen.

$$tc = \max\left(\frac{\Delta p \cdot Rc_{int}}{\sigma_{all} \cdot \eta_w - 0.6 \cdot \Delta p}; \frac{\Delta p \cdot Rc_{int}}{2 \cdot \sigma_{all} \cdot \eta_w + 0.4 \cdot \Delta p}; 1.6 \text{ mm}\right) \quad (19)$$

The internal radius is updated with the value resulting from $Rc_{int} = R_{str} - tc$ and Equation (19) is applied iteratively until tc converges within an assigned threshold.

- Similarly, the thickness of vessel endcaps (te) is calculated according to [38] using the formula in Equation (20), in which the function $k(f_{end})$ is defined in Equation (21) and the second term is introduced to guarantee the applicability of the first expression.

$$te = \max\left[k(f_{end}) \cdot \frac{\Delta p \cdot Re_{int}}{\sigma_{all} \cdot \eta_w - 0.1 \cdot \Delta p}; 5 \cdot 10^{-4} \cdot L; 1.6 \text{ mm}\right] \quad (20)$$

$$k(f_{end}) = \begin{cases} \frac{2+f_{end}^{-2}}{6} & \text{for } 0.0005 \leq te/L < 0.002 \\ 1 & \text{for } te/L \geq 0.002 \end{cases} \quad (21)$$

At the first step it is assumed that $Re_{int} = Rc_{int}$, then the internal radius is updated with the value resulting from $Re_{int} = R_{str} - te$ and Equation (20) is iterated until the convergence of te ;

- The obtained thickness values allow to calculate the longitudinal mass distributions as well as the total mass of the tank, taking the structure, the insulation layer, and assuming the whole internal volume can be filled with LH₂;
- Given the mass distribution, it is possible to calculate both the maximum (tensile) and minimum (compressive) axial local stress and perform the verifications given in Equation (22). In this latter, the first line is the comparison between the limit longitudinal tensile stress, resulting from both the internal pressure (first term in brackets) and the bending moment, and the strength of the welded material, whereas the second line is the local buckling verification for the cylindrical part of the vessel at ultimate load factors. For buckling design, a null value was assigned to Δp since a positive value reduces the compressive stress in tanks' shells. This assumption is conservative, since a minimum Δp of about 20% of external atmospheric pressure is constantly kept by means of check valves that prevent the inversion of mass flow in the outlets. Column buckling verification was implemented too, but it is not reported here for conciseness, since local buckling is more critical in most of the observed cases.

$$\left\{ \begin{array}{l} \left(\frac{\Delta p \cdot Rc_{int}}{2 \cdot tc} - 0.2 \cdot \Delta p\right) + n_r \frac{B_{max} \cdot R_{str}}{I} \leq \sigma_{all} \cdot \eta_w \\ \max\left[1.5 \cdot n_r \frac{B_{max} \cdot R_{str}}{I_c}; 1.5 \cdot n_x \frac{N_{max}}{\pi(R_{str}^2 - Rc_{int}^2)}\right] \leq \Delta_b \left(\frac{L}{D_{str}}, \frac{d_{supp}}{L}, te\right) \cdot \frac{0.125}{FS} \cdot E \cdot \frac{tc}{R_{str}} \end{array} \right. \quad (22)$$

The variables in Equation (22) not yet introduced are:

- B_{max} , the maximum bending moment, calculated considering both the longitudinal mass distribution varying along the tank and the distance between the supporting frames (d_{supp});
- N_{max} , the maximum compressive axial load;

- I_c , the inertia moment of the central tube;
- FS , a design factor defined depending on the ratio between the predicted buckling stress (σ_b) and the yielding stress as in Equation (23);

$$FS = \begin{cases} 2 & \sigma_b \leq 0.55 \cdot \sigma_y \\ 2.407 - 0.741 \frac{\sigma_b}{\sigma_y} & \text{for } 0.55 \cdot \sigma_y < \sigma_b < \sigma_y \\ 1.667 & \sigma_b \geq \sigma_y \end{cases} \quad (23)$$

- E , the modulus of elasticity of the structural material;
- Δ_b , a correction function, depending on the length-to-diameter ratio (L/D_{str}), the nondimensional distance between supports (d_{supp}/L), and endcap wall thickness (te), derived from FEM analyses as described in Section 2.4.1.

The buckling strength, i.e., the terms on the right-hand side of the Equation (22) second and third lines, is derived from the design-by-formula approach given by the “Alternative Rules” of ASME Boiler and Pressure Vessel Code [39] and is the most recurring formula for the tank geometries considered here. The whole set of formulas obtained by varying geometric parameters, such as thickness-to-radius and length-to-radius ratios, was implemented in the design procedure but is not reported here for the sake of conciseness; the reader interested in such details can refer to Section 4.4.12 of [39].

- If any of the previous verifications is not fulfilled, the thickness tc is recalculated within an iterative loop in which masses and inertial loads are updated at each step.

The following aspects are worth mentioning:

- Equation (19) as well as the first line of Equation (22) are valid for cylindrical tubes with thickness-to-radius lower than 0.5, whereas Equation (17) is valid for endcaps with thickness-to-radius lower than 0.356. The fulfilment of these constraints is checked at the end of the sizing procedure;
- The third line of Equation (22) is valid for values of $\frac{R_{str}}{tc} \leq 1000$ ([39]), higher values require a design-by-analysis approach to assess adequate protection against buckling;
- A buckling verification for endcaps was not implemented since they are not subject to compression, as usually happens for tanks that undergo external pressure loads;
- According to [26], hydrogen tanks need to be verified also at the burst condition, defined as a load case in which only a pressure load equal to twice the limit design pressure (Δp) is applied. In such condition, it is required that the tank can carry the load without catastrophic failures. In the procedure adopted here, Equation (17) introduces a safety factor of 3.5 between the maximum allowable stress and the ultimate strength of the material, hence burst condition is self-verified;
- For the case of aluminium alloy AA2219, the authors of [26] report a fatigue analysis for a LH₂-propelled transport aircraft assuming 50,000 service hours corresponding to 10,000 ground–air–ground cycles. For such case, a 172 MPa limitation to circumferential stress of a tank’s skin results in a life reduction factor of 4, i.e., a fatigue life of 40,000 cycles. In the case considered here, taking AA2219 data in Table 4 into account, the allowable value resulting from Equation (17) is 145 MPa, well below the limit indicated above.

2.4.1. Validation of the Structural Model with FEM Analyses

The results of the analytical structural model presented in Section 2.4 were compared with FEM analyses considering the two test cases presented in Table 5, where the last row indicates the value of the correction function Δ_b introduced in Equation (22). This was obtained by means of FEM analyses aiming to compare the critical load obtained for buckling eigenvalue equal to unity with the estimation provided by the right-hand term in the 2nd line of Equation (22) without any correction. The FEM simulation campaign was carried out using the two test cases reported in Table 5 as baseline configurations,

and varying the parameters that it depends on, in order to cover a wide range of cases of interest.

Table 5. Input and output of the analytical model for two test cases.

Input	Test Case #1	Test Case #2
D_{str} [m]	3.00	3.00
L/D_{str} [–]	1.00	2.00
f_{end} [–]	0.60	0.60
d_{supp}/L [–]	0.70	0.90
p_{int}/p_{ref} ($p_{ref} = 144.8$ kPa)	1.40	1.00
t_{ins} [mm]	100	100
Structural material and characteristics	AA 2219 (Table 4)	AA 2219 (Table 4)
Insulation material and characteristics	Polystyrene foam (Table 3)	Polystyrene foam (Table 3)
Output	Test Case #1	Test Case #2
t_c [mm]	2.1	2.4
t_e [mm]	1.7	3.0
Tube structural mass [kg]	166	383
Endcaps (2) structural mass [kg]	97	175
Total insulant mass [kg]	132	207
Total tank empty mass [kg]	395	765
Internal volume [m ³]	29.6	50.7
Allowable tensile stress on welded joints [MPa]	159	159
Nominal buckling strength (long cylinders) [MPa]	6.6	7.6
FEM derived correction factor Δ_b [–]	0.50	0.83

The two test cases were created in order to underline the differences between structural sizing dominated by tensile or buckling strength. In fact, the 1st case is a tank with a shorter cylindrical part and a higher internal pressure, whereas the 2nd tank is longer and has a larger unbraced length; hence, the design of the 1st cylinder is driven by the circumferential stress acting on welded joints, whereas the 2nd cylinder is designed to withstand buckling loads.

The finite element mesh of each tank is made up of shell elements only; non-structural elements, such as hydrogen and the insulation layer, were modelled as non-structural masses. Different loading conditions were considered as combinations of inertial and pressurisation loads for static sizing verifications. For the bending-induced buckling analyses, only the ultimate downward inertial load was considered; thus, ignoring the beneficial effect of pressurisation on critical load evaluations; the latter was predicted by means of an eigenvalue analysis, according to Equation (24), where P_{dead} is a pre-existing applied load (preload or dead load) and ΔP is the perturbation load introduced in the buckling analysis step. For these analyses, a null preload and a perturbed load equal to the ultimate downward inertial load were considered. Normally, the lowest positive eigenvalue is of interest.

$$P_{cr} = P_{dead} + \lambda_i \cdot \Delta P \quad (24)$$

For all the analyses, the structural connections between the tank and the fuselage were modelled as multi-point constraints. In details, at the two sections where the structural supports are located, the points on the longitudinal axis were designated as “master nodes” and multi-point constraint relationships were created with the “slave nodes” located on the cylindrical surface. For one of the master nodes the degrees of freedom associated to radial,

azimuthal, and axial displacements are inhibited, whereas the other one differs from the previous only for the axial displacement, which is allowed. Torsion is inhibited by having imposed zero rotation with respect to the longitudinal axis at these points. The system so defined is, thus, isostatic.

The obtained results are summarised in terms of safety factors for both tensile and buckling strength, with a good accordance between the model implemented and FEM analyses (see Table 6). In addition, looking at the values assumed by the safety factors, it can be observed how the design test case #1 is dominated by the strength criterion, whereas test case #2 is driven by buckling.

Table 6. Safety factors calculated for the structural test cases.

Safety Factors	Test Case #1		Test Case #2	
	ASME ([38,39])	FEM	ASME ([38,39])	FEM
Tube—longitudinal tensile stress [–]	1.99	2.03	3.18	3.18
Tube—circumferential tensile stress [–]	1.00	1.00	1.69	1.67
Endcap—tensile stress [–]	1.00	0.98	2.66	2.55
Tube Buckling	Buckling stress [–]	1.81	1.32	1.35
	1st Eigenvalue [–]	-	2.55	-

Figure 13 shows the lowest buckling modes for both test cases; the effective length of the column is comparable to the distance between supports. For the shorter tank, the buckling eigenvalue is about 2.55, whereas for the longer one it is about 1.35; this confirms what was said previously, that the test case 1 is dominated by static sizing, whereas for test case 2 bending-induced buckling is dominant.

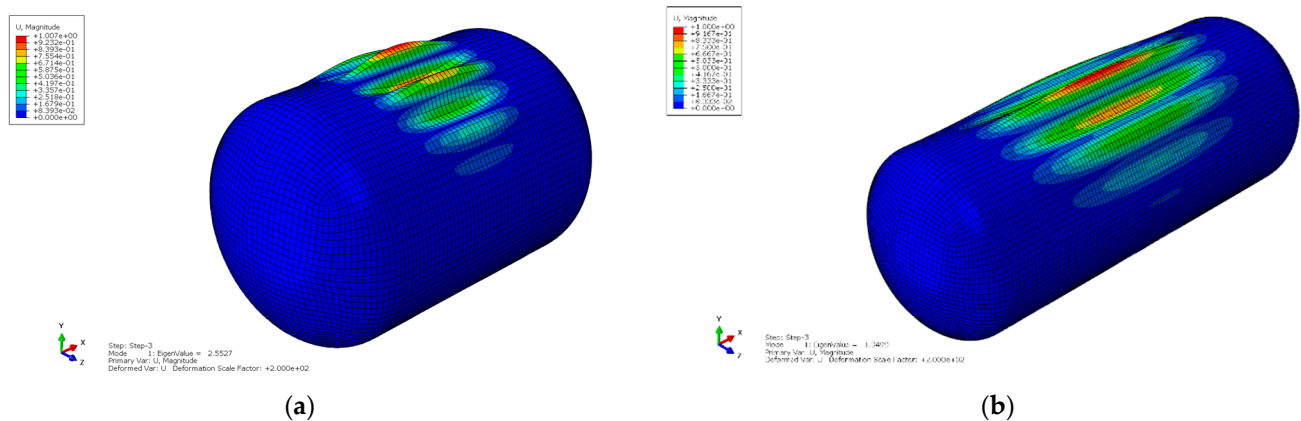


Figure 13. Visualisation of buckling analysis results for test cases #1 (a) and #2 (b) under ultimate downward inertial loads ($n_r = 4.5$).

2.5. Thermodynamic Analyses

The tank thermodynamic analysis was carried out according to the procedure presented in [24]. The thermodynamic analysis objective is to determine weight, volume, and pressure of the LH₂ contained in the tank, at each point of the mission. This computation is not as simple as for the traditional fuel, since the density of the saturated H₂ is variable with the tank state, and because of the eventuality of venting in case of overpressure. In addition, the analysis needs to check that the H₂ pressure never falls under the minimum pressure to avoid contamination from atmospheric oxygen ([25,33]).

2.5.1. Tank Thermal State Dynamics

Since the H₂ cryogenic storage condition was considered, the internal tank temperature is always lower than the environmental one. This fact generates a heat flux from the environment to the stored H₂, which leads to a variation in temperature and pressure of the fluid. The laws governing the pressure variation over time in a saturated H₂ homogeneous fluid, in the presence of a heat flux, are reported in [31]. The present paper assumes that the “Passive thermodynamic venting system” case is valid (formula n. 8 in [31]). However, for the sake of simplicity, it is assumed that only the gaseous phase is vented, hence neglecting the refrigeration effect due the vented liquid phase. Therefore, the aforementioned formula is simplified in Equation (25).

$$\frac{dP}{dt} = 2 \frac{\Phi}{V} \left[Q - m_o (h_g - h_l) \left(X_o + \frac{\rho_g}{\rho_l - \rho_g} \right) \right] \quad (25)$$

$$m_o = m_{fuel} + m_{vent} \quad (26)$$

$$X_o = \frac{m_{vent}}{m_o} \quad (27)$$

$$\Phi = \frac{1}{\rho \left(\frac{\partial u}{\partial P} \right)_{\rho}} \quad (28)$$

In Equation (25), Q is the heat flux toward the H₂, V is the tank volume, h_g and h_l represent the unit mass enthalpy of the gaseous and liquid phase, respectively, whereas ρ_g and ρ_l are the respective densities.

Because of the presence of the venting valve, the outgoing mass flow (m_o , [kg/s]) is represented by the sum of the mass flow of the liquid phase, headed to the engines (m_{fuel}), and the mass flow of the gaseous phase, expelled by the venting valve (m_{vent}), as reported in Equation (26). The quality of the outgoing mass flux (X_o) is the ratio between the gaseous phase mass flow and the total outgoing mass flow (Equation (27)).

According to [25,31], Equation (25) shows a factor 2, in order to take the fluid stratification into account, which is present if proper fluid mixing devices are omitted. The fluid stratification leads to higher pressure variations for a given energy input, if compared to a case in which homogeneous fluid is assumed.

The term Φ in Equation (25) is the “energy derivative”, defined as in Equation (28). More details about its estimation are reported in Appendix A.

The pressure variation inside the tank is determined using Equation (25) in a Eulerian integration in parallel with the mission analysis simulation, as explained in Section 2.6. The mission simulation determines the environmental conditions and the fuel flow (m_{fuel}).

The venting valve mass flow (m_{vent}) in Equation (25) is determined for the three conditions summarised in Equation (29):

- While the tank pressure is lower than the venting pressure $P < P_{vent}$, m_{vent} is set to zero.
- When $P \geq P_{vent}$, the venting valve is activated. In this paper, the venting valve mass flow (m_{vent}) is considered variable in such way that the pressure inside the tank is kept constant. The computation of m_{vent} is completed imposing $dP/dt = 0$ in Equation (25), obtaining the second case of Equation second case of Equation (29) (details in Appendix B). By substituting the computed m_{vent} in Equation (25)), the pressure will be kept constant over time.
- While $P \geq P_{vent}$, an increase in fuel consumption, or a decrease in environmental temperature, will cause a pressure decrease; however, since dP/dt was set to zero, this condition leads to a solution where $m_{vent} < 0$. In this condition, the computed mass flow is clearly non-physical, since the venting valve is a one-way item. For a correct

consideration of this last case, when simultaneously $P \geq P_{vent}$ and $m_{vent} \leq 0$, m_{vent} is set to zero:

$$m_{vent} = \begin{cases} 0 & P < P_{vent} \\ \left(-b + \sqrt{b^2 - 4ac}\right) / (2a) & \text{if } P \geq P_{vent} \text{ and } m_{vent} > 0 \\ 0 & P < P_{vent} \text{ and } m_{vent} \leq 0 \end{cases} \quad (29)$$

where:

$$a = 1 + \frac{\rho_g}{\rho_l - \rho_g} \quad (30)$$

$$b = m_{fuel} + 2m_{fuel} \frac{\rho_g}{\rho_l - \rho_g} - \frac{Q}{h_g - h_l} \quad (31)$$

$$c = m_{fuel}^2 \frac{\rho_g}{\rho_l - \rho_g} - m_f \frac{Q}{h_g - h_l} \quad (32)$$

2.5.2. Tank Heat Flow

The heat flow across the tank walls (Q in Equation (25)) is computed considering three main thermal exchange stages: the external heat exchange, the heat conduction across the tank insulation, and the heat exchange inside the fluid.

For the sake of simplicity, the following assumptions were introduced:

- (a) Each tank has the same structure shown in Figure 7 and it is assumed that the foam insulation is in direct contact with the external air, which flows at the aircraft flight speed.
- (b) The heat exchange across the tank bulkheads occurs in the same way as for the external diameter. This assumption is less conservative, because the temperature inside the fuselage, in cruise, could be higher than the external one (non-conservative). Moreover, the heat exchange phenomena at the boundary of the insulation inside the fuselage is natural convection, that is different from the forced convection occurring at the boundary with the external environment (conservative). The heat exchange across the bulkheads, however, is strongly dependent upon the passenger compartment wall design, which is out of the scope of this work, so the assumption is considered valid.
- (c) The computation of thermal exchange surfaces was simplified, assuming that the boundaries of every heat exchange phenomenon have the shape of a cylinder of the same overall length of the tank with plane bulkheads.

The external heat exchange is characterised by forced convection and thermal radiation between the external skin of the insulation and the environment; these phenomena are considered by means of the equations reported in [25]. For the convection, we have:

$$Nu = \frac{h_{conv} \cdot L}{k_{air}} = 0.03625 \cdot Pr^{0.43} \cdot Re^{0.8} \quad (33)$$

$$Pr = \frac{\mu_{air} \cdot Cp}{K_{air}} \quad (34)$$

$$Re = \frac{\mu_{air} \cdot v \cdot L}{K_{air}} \quad (35)$$

where Nu , Pr , and Re are the Nusselt, Prandtl, and Reynolds number typical of this phenomenon, h is the heat transfer coefficient [$W/(m^2 K)$], L is the tank length, k_{air} is the air thermal conductivity, μ_{air} is the dynamic viscosity of the air, Cp is the air specific heat at constant pressure, and v is the airspeed.

The radiation to the environment is characterised by the following formula [25,41]:

$$h_{rad} = \sigma \varepsilon \left(T_{skin}^2 + T_{atm}^2\right) (T_{skin} + T_{atm}) \quad (36)$$

where h_{rad} is the heat transfer coefficient of the phenomenon, T_{skin} is the aircraft skin temperature, T_{atm} is the environment temperature, σ is the Stefan–Boltzmann constant, and ε is the emittance of the radiating surface, which is set to 0.95, corresponding to a white painted surface [25]. As for the assumptions (a), (b), and (c), the total external resistance is computed as in Equation (37), where S_{ext} is the total external surface of the tank at the external foam interface.

$$TR_{ext} = \frac{1}{S_{ext} (h_{conv} + h_{rad})} \quad (37)$$

The thermal resistance of a cylindrical foam layer TR_{ins} (tube-like problem) is given by the Equation (38), as reported in [25,42]:

$$TR_{ins} = \frac{1}{2\pi l} \frac{\ln\left(\frac{r_o}{r_i}\right)}{K_{ins}} \quad (38)$$

where r_i and r_o are the foam internal and external radius, respectively, l is the cylinder length, and K_i is the thermal conductivity of the foam. Equation (38) assumes that the foam thermal conductivity is constant along the radius, but this condition is not verified due to the thermal gradient inside the foam, and the foam's thermal conductivity dependence upon temperature. Because of this fact, it is necessary to split the foam thickness into a number of concentric shells which were set to 40, according to [25]. The heat exchange inside the fluid is characterised by the natural convection in the liquid and gaseous phases. For the liquid phase, the following equations were considered:

$$Nu = 0.0605 Ra^{1/3} \quad (39)$$

$$Ra = \frac{g \beta \Delta t H^3 Pr}{\nu} \quad (40)$$

$$Pr = \frac{\mu Cp}{K} \quad (41)$$

$$h_l = \frac{Nu K}{H_l} \quad (42)$$

where all quantities are relative to the liquid phase, Nu , Ra , Pr , are the Nusselt, Raleigh, and Prandtl numbers for the natural convection inside the liquid H_2 , h_l is the heat transfer coefficient of the phenomenon, H_l is the level of the liquid part inside the tank, expressed as height from the bottom of the tank, K , Cp , β , and ν are, respectively, the thermal conductivity, the specific heat at constant pressure, the coefficient of volumetric thermal expansion, and the cinematic viscosity of the liquid H_2 , whereas Δt is the temperature difference between the tank wall and the bulk of the liquid H_2 . β was derived as reported in Appendix C. For the gaseous phase the following equations were considered ([25]):

$$Nu = 17 \quad (43)$$

$$h_g = \frac{Nu K}{H_g} \quad (44)$$

where all quantities are relative to the gaseous phase, Nu is the Nusselt number for the natural convection inside the gaseous H_2 , h_g is the heat transfer coefficient of the phenomenon, H_g is the level of the gas inside the tank, expressed as distance from the top of the tank, and K is the thermal conductivity of the gaseous phase. As for assumptions (a), (b), and (c), the total internal thermal resistance is computed as in Equation (45), where S_l and S_g are the tank surfaces in contact with the liquid and gaseous phase, respectively.

$$TR_{int} = \frac{1}{S_l h_l + S_g h_g} \quad (45)$$

The heat flow (Q) evaluation is computed using the method reported in [24]. The method assume that all the above-mentioned thermal resistances are in series, so the heat flow that crosses each resistance is the same. It is possible to write a linear system of equations in the form $AX + B = 0$, as in Equation (46), in order to determine Q and all the temperatures at each tank thermal stage interface:

$$\begin{pmatrix} 1 & 0 & 0 & TR_{ext} \\ -1 & 1 & 0 & TR_{ins1} \\ 0 & -1 & 1 & TR_{ins2} \\ \dots & \dots & \dots & \dots \\ 0 & 0 & -1 & TR_{int} \end{pmatrix} \begin{pmatrix} T_{skin} \\ T_{ins1} \\ T_{ins2} \\ \dots \\ Q \end{pmatrix} + \begin{pmatrix} -T_{ext} \\ 0 \\ 0 \\ \dots \\ T_{h2} \end{pmatrix} = 0 \quad (46)$$

Since the thermal resistance TR of each thermal stage is dependent upon the temperatures at the thermal stage interfaces, the system is solved with an iterative procedure. It starts with temperature initialisation values identical to the environmental one, and lasts until the convergence on the temperatures at the outer skin and LH₂ interfaces, with a tolerance of 0.5 K.

2.6. Mission Analyses

2.6.1. Reference Aircraft and LH₂ Aircraft Derivation

The box-wing aircraft used as a baseline reference for the study of integration of hydrogen propulsion is one of the results of the European project PARSIFAL ([6–10]). Carried out between 2017 and 2020, PARSIFAL has been funded under the Horizon 2020 programme, with the goal of studying the adoption of box-wing aircraft in the medium-range air transport sector, assessing its operational and environmental impact. One of the objectives of PARSIFAL was to exploit the theoretical aerodynamic superiority of the box-wing lifting system to increase the number of passengers with respect to direct competitors, i.e., Airbus 320 or Boeing 737 family craft, while complying with the same airport constraints and, above all, reducing the fuel consumption per passenger-kilometre ([43]). The designed aircraft has a box-wing architecture with the following main features: a number of passengers equal to 308, 66% more than the conventional competitor; a wingspan equal to 36 metres, and compatible with ICAO category ‘C’ airport aprons ([44]); and a maximum reduction in block fuel per passenger-kilometre equal to 22% compared to the conventional competitor ([45]). Figure 1 presents the final configuration of the PARSIFAL box-wing aircraft, whereas its main characteristics are reported in Table 7; for further details on the study and design of the box-wing aircraft developed within the PARSIFAL project, please refer to [12,43,45].

Table 7, in addition to reporting the main characteristics of the box-wing aircraft used as a baseline for this LH₂ propulsion integration study, also reports how this integration was achieved by modifying the reference aircraft. It should be underlined that the strategy to develop the LH₂ aircraft used in this research is based on the retrofit of the baseline aircraft; this involves a number of constrained design choices that are described hereafter. First, the shape of the aircraft and its main structure are kept the same as that of the baseline. This implies two major effects on the overall aircraft design: firstly, the mass of the main structures of the aircraft, i.e., lifting system, fins, landing gear, and fuselage, is the same as that of the baseline aircraft. Regarding the fuselage structure, the following assumption is made in this study: at this preliminary level it is assumed that the mass of structural components removed to allow the LH₂ tank installation (e.g., floor beams and trusses in the case of the full-section layout) is compensated by the introduction of new structures, such as the frames needed to support the tanks; in other words, the mass balance resulting from the installation of tanks inside the fuselage is almost zero. Secondly, since the external shape of the aircraft is the same as the baseline, the aerodynamic performance is also the same as calculated for the PARSIFAL box-wing aircraft. As the LH₂ tanks are located inside the fuselage, no modifications to the aircraft shape are foreseen; therefore,

no new calculations are needed to evaluate the aircraft aerodynamics. All the results on aerodynamic performance were taken from [43].

Table 7. Characteristics of the LH₂ aircraft derived by the reference aircraft.

Parameter	Reference Aircraft (PARSIFAL)	Retrofit Methodology	LH ₂ Aircraft
Passenger capacity	308	Full-section: depending on tanks' length Part-section: unchanged	Full-section: variable (≤ 308) Part-section: 308
Cabin crew	7	Depending on passenger capacity	Variable (≤ 7)
Number of containers	12	Depending on tank length	Variable (≤ 12)
Empty mass [kg]			
• Overall engine mass	13,676	Increased by 1% (see Section 2.1.1)	13,813
• Structural mass	30,996	Unchanged	30,996
• System mass	9466	Depending on passenger capacity (according to [46])	Variable (air conditioning, containers)
• Operating mass	14,180	Depending on passenger capacity (according to [46])	Variable
• Tanks and fuel system mass	548	Increase in total empty mass of LH ₂ tanks	Variable
Fuel mass [kg]	27,000 (Kerosene)	Calculated	Variable (LH ₂)
Max. take-off weight [kg]	125,126	Calculated	Variable ($\leq 125,126$)
SFC [kg/kg/s]	1.39×10^{-4}	Decreases by 64.71% (see Section 2.1.1)	4.87×10^{-5}
Drag polar curve	See Figure 14	Unchanged	See Figure 14
Harmonic range [km]	5722 km	Calculated	Variable

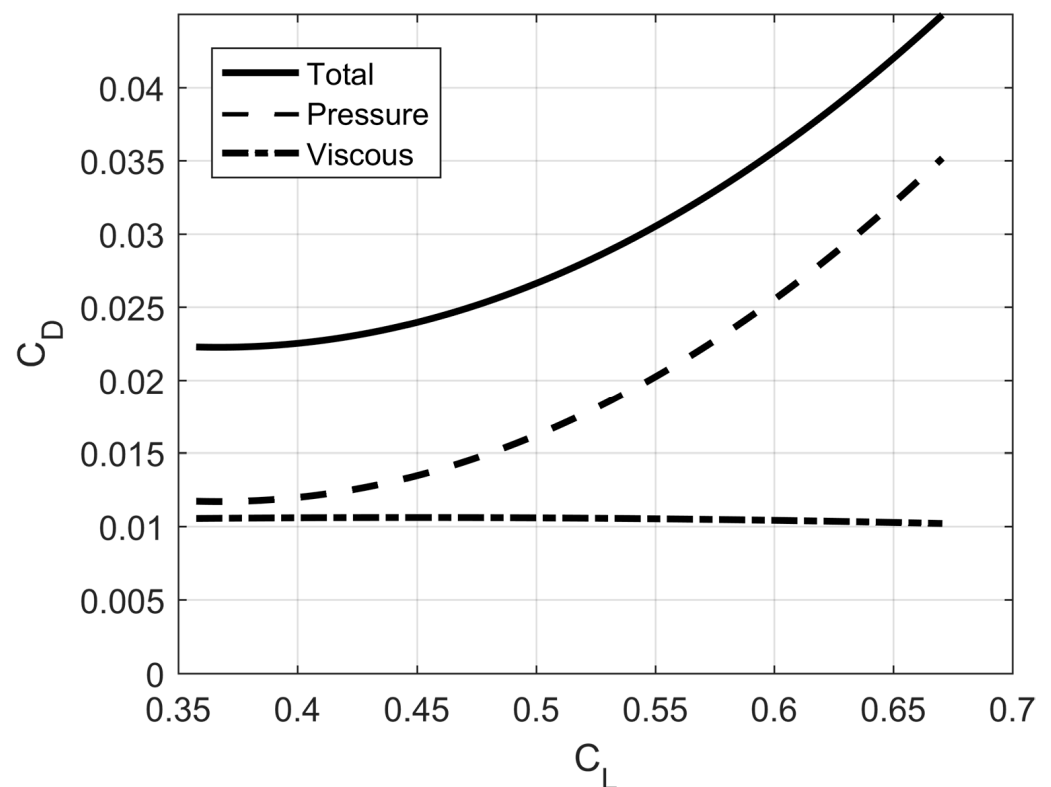


Figure 14. Drag polar curve of the box-wing aircraft studied in the project PARSIFAL ([45]).

Concerning the retrofit of the propulsion system, as mentioned in Section 2.1.1, the assumption made is that the turbofan engine of the retrofitted aircraft is the same as the baseline aircraft, except for the introduction of a dedicated heat exchanger.

The main modifications with respect to the baseline box-wing aircraft concern the internal design of the fuselage. In fact, as already explained in Sections 2.1.2 and 2.3, the cylindrical tanks employed in this study are placed inside the fuselage; this is completed at the expense of the internal volume available to house the payload. This aspect, in addition to the demonstrated larger aerodynamic efficiency of the box-wing architecture, was decisive in the choice of the baseline aircraft to retrofit. Indeed, the PARSIFAL fuselage was designed with a different shape compared to conventional competitors [43]; in particular, the cabin section is enlarged to accommodate 8 passengers per row, and the aft section is designed to maximise the internal volume. Thanks to this fuselage design, it is possible to achieve the above-mentioned payload increase obtained with the PARSIFAL aircraft. The large internal volume provided by this new fuselage design can enable the installation of the required number of tanks in the fuselage, without resulting in compromising penalties in terms of reduction in the number of passengers or in the maximum range. In fact, it is well known that a major drawback of LH₂ tanks is related to the high volume required, and excessive reductions in payload and/or range could jeopardise the effectiveness of the introduction of the LH₂ propulsion system. In order to evaluate the operational capabilities of the retrofitted LH₂ box-wing aircraft, extensive sensitivity studies have been carried out on the number and size of on-board tanks, and on the related impact in terms of payload and range reductions, as reported in detail in Section 3.

The possibility of reducing the number of passengers and/or containers to provide internal fuselage volume to house the LH₂ tanks, involves the need to re-evaluate the weight of some on-board systems and operating items that are directly correlated to the number of passengers. In particular, with respect to the baseline aircraft, for each value of number of passengers evaluated for the retrofitted aircraft, the masses of the interior furnishings, the cabin crew, the seats, the galleys and toilets, the cabin air conditioning system, and the cargo containers, were re-evaluated, as indicated in [46].

The main constraint resulting from the choice to retrofit a baseline aircraft is imposed on the MTOW. Since the main structure of the lifting system and of the fuselage was sized considering the maximum take-off weight calculated in PARSIFAL [47], it is necessary to maintain the same limit on the maximum take-off weight also in this study.

2.6.2. Mission Description and Simulation

This reference mission used to assess the performance of the box-wing aircraft was divided into segments with their own characteristics, as described in the following and schematically shown in Figure 15:

- Ground holding: is a 30 min standby phase carried out with the engines switched off, which is necessary for fuelling and for other aircraft preparation operations ([24]).
- Taxi-out: it is conducted according to the Landing and Take-off (LTO) cycle specifications defined by ICAO ([48]); its duration is equal to 13 min, half of the total taxi in and out duration, in which the engine power setting is set to 7% of maximum thrust, corresponding to the idle condition.
- Take-off: as for the taxi-out phase, the take-off was also computed by using the ICAO engine emissions database specifications; specifically, the duration of the manoeuvre is set to 0.7 min in which the engine power setting is 100%.
- Take-off path: this segment of the mission acts as a link between the on and off ground mission stages; the take-off flight path starts 35 ft above the ground and ends when the height of 1500 ft is reached. In this stage, the aircraft is configured for starting the climb ([43]).
- Climb: this stage is divided into three main phases in which the aircraft accelerates and gains altitude, as suggested by the flight programme described in [49]; the climb ends as the altitude of the cruise condition is reached.

- Cruise: this segment is performed with a constant speed–constant altitude flight programme; the reference cruise condition is $h_{cr} = 11,000$ m and $M_{cr} = 0.79$.
- Descent: the descent is performed with an imposed speed profile and a constant rate of descent, as described in [43].

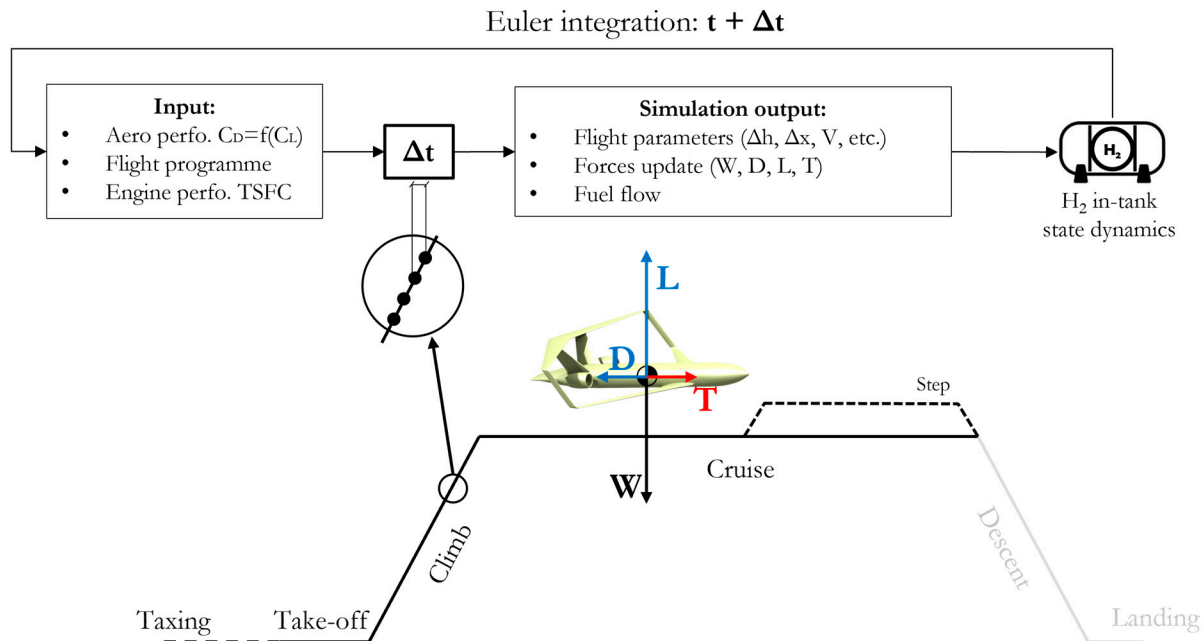


Figure 15. Standard mission simulation scheme.

The phases outlined above represent what is known as standard mission. In this study, the standard mission was simulated by time-integrating the equations of motion of the aircraft by means of the Euler algorithm, as reported in [45].

In addition to the standard mission, there is a further part of the mission that must be considered when designing an aircraft; this additional phase, called diversion, takes off-design situations, such as weather or technical emergencies, into account. Therefore, diversion is supposed to start after an emergency occurring close to the planned landing and it is meant to divert the aircraft to a new airport, defined as the alternate. Thus, the diversion phase consists of a climb, a cruise at diversion altitude, a descent, a holding phase of 40 min and a landing. An amount of reserve fuel, equal to 5% of the calculated total fuel, is then added at the end of the mission analysis.

In this study, the diversion is not simulated as done for the standard mission phases, and the fuel consumption during the diversion phase is estimated on the basis of the performance data available for the baseline box-wing aircraft ([43]). This simplification was introduced to reduce the simulation time, which for a LH₂-propelled aircraft is longer than that for a conventional propulsion aircraft, since at each time step both the fuel flow and the state dynamics of the hydrogen inside the tanks vary.

More in detail, the amount of fuel required to perform the descent and diversion, as well as for reserve, is calculated a priori by interpolating the available data of the reference box-wing ([43]) on input values related to the LH₂ aircraft under investigation. Such amount of fuel sets a minimum threshold for the LH₂ to be contained in the tanks at the end of cruise phase. Therefore, the standard mission is simulated until the total fuel in the tanks reaches such threshold value, then the simulation stops and the aircraft performance, such as the flight distance, is obtained in output without the need to iterate.

It is worth remembering that the LH₂ consumption during flight takes both the consumption needed to feed the engines and the amount of H₂ expelled by venting into account, as described in detail in Section 2.4.1. In addition, the mission simulation is prematurely stopped if the pressure inside the tanks drops below the minimum safety pressure.

This coupled mission–thermodynamic analysis depends on the strategy which defines the fuel flow supplied by each tank. For example, venting and pressure drop could be actively contrasted implementing a flow control law depending on the instantaneous internal pressure. For the sake of simplicity and to save computational time, in this preliminary study the same fuel flow value \dot{m}_{ft} was assumed for all the active tanks, i.e., those in which LH₂ is not depleted. At each time step, \dot{m}_{ft} is calculated as in Equation (48), where \dot{m}_{fe} is the fuel flow requested from all the engines and n_{at} is the number of active tanks. This latter is updated at each time step comparing the quantity of LH₂ left in each tank with a minimum threshold value (70 kg, corresponding to 1 m³).

$$\dot{m}_{ft}(t) = \frac{\dot{m}_{fe}(t)}{n_{at}(t)} \tag{47}$$

3. Discussion of Results from Sensitivity Analyses

The following sections report the results of several sensitivity analyses carried out under an aircraft performance-oriented perspective, i.e., using in most of the cases the mission range as the main figure of merit.

3.1. Studies Concerning Tank Materials and Technologies

3.1.1. Sensitivity to Structural Materials

The effects of the several design parameters on the structural design of non-integral tanks made of unstiffened shells LH₂ as the one depicted in Figure 2, were investigated through the sizing procedure described in the previous section considering the different materials reported in Table 4. The figure of merit considered here is the structural mass fraction (μ_{str}) defined in Equation (48), where M_{str} is the total mass of the tank’s walls, V_{int} is the gross internal volume of the tank, and ρ_{LH} is the density of the LH₂.

$$\mu_{str} = \frac{M_{str}}{V_{int} \cdot \rho_{LH}} \tag{48}$$

Figure 16 shows the results of the sensitivity analysis for assigned values of external diameter of the tube, $D_{str} = 3$ m, and thickness of the insulation layer, $t_{ins} = 0.1$ m, which contributes to the inertial loads acting on the structure. The parameters considered are:

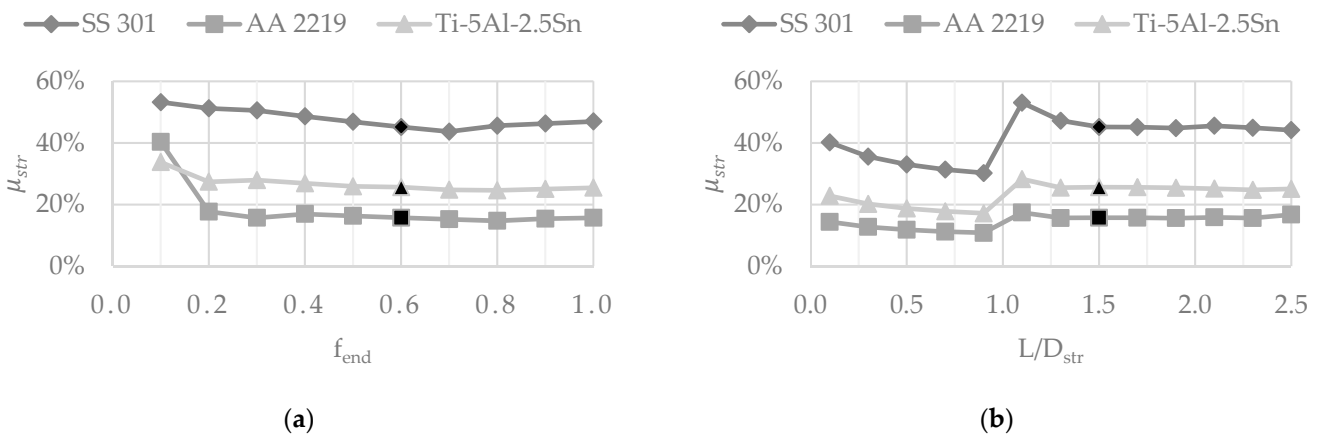


Figure 16. Cont.

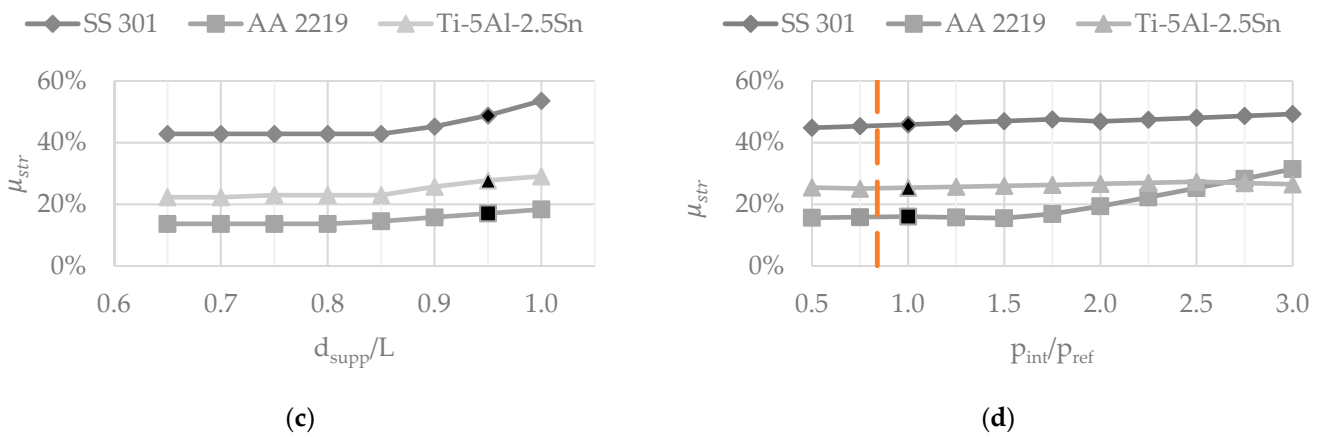


Figure 16. Structural mass fraction (μ_{str}) for different materials and design parameters: (a) f_{end} , (b) L/D_{str} , (c) d_{supp}/L , and (d) p_{int}/p_{ref} .

- f_{end} , the aspect ratio of endcaps (Figure 16a);
- L/D_{str} , the aspect ratio of the cylindrical tube (Figure 16b);
- d_{supp}/L , the ratio of distance between supports and tube length (Figure 16c);
- p_{int}/p_{ref} , the ratio between the internal pressure and the reference value of 144.8 kPa (Figure 16d);
- In each chart, the points highlighted in black indicate the values assigned to the parameters when they are not the object of sensitivity analyses. As a first general comment.

Figure 16 highlights how, in most of the cases, the lower density of the aluminium alloy makes this latter a better compromise than steel or titanium alloy. More in detail, the following remarks can be pointed out:

- Concerning f_{end} , for each selected material it is possible to prescribe a minimum value that avoid the increase in μ_{str} . In fact, at low values the endcaps get thicker (see the f_{end} effect in Equation (20)) and a snowball effect is produced on the structural mass, as the increase in associated inertial loads pushes towards greater tube thickness to avoid buckling conditions. If, instead, higher f_{end} values are considered, endcaps walls do not grow in thickness, but the contained LH₂ mass grows linearly with f_{end} , which determines higher inertial loads and eventually produces a slight but constant increase in tube thickness;
- For L/D_{str} , values close to 1 minimise μ_{str} , whereas higher values amplify the inertial loads, causing the increase in tube thickness as previously explained. For lower values, the slight increase in μ_{str} is only due the reduction in internal volume available for LH₂ mass.
- The effect of increasing d_{supp}/L , visible only for aluminium and titanium alloys, is a higher peak value of the compressive axial load (N_{max}), which is one of the inputs of the buckling verification in Equation (22). Values of d_{supp}/L larger than 1 are possible, meaning that the supporting frames are connected to the endcaps.

Considering p_{int}/p_{ref} , for any of the structural material there are no benefits in increasing the internal pressure, since the main effect would be a reduction in LH₂ density (see Figure 3), hence an increase in μ_{str} . The dashed vertical line in Figure 16d indicates the constraint resulting from setting the minimum value of Δp to 20% of external atmospheric pressure.

Therefore, the present analysis allows to draw some design guidelines:

- It is suggested to prefer the aluminium alloy AA2219 as structural material;
- A f_{end} value greater than 0.4 should be chosen. In this study, the value 0.6 was selected in accordance with [26], where a value of 1/1.6 is suggested to minimise Direct Operating Costs;

- A L/D_{str} value outside the (1, 1.5) interval should be selected, moving towards higher or lower values depending on the required amount of LH₂. In the following cases, a value of 1.5 was adopted;
- A d_{supp}/L value lower than 0.8 should be considered. In the following cases, a value of 0.8 has been adopted.

Additional observations can be made for the welding efficiency (η_w) and the operating temperature, which are both expected to influence the design according to Equations (17), (19) and (20). Results of the analyses, not reported here for brevity, indicate that the effect of η_w in the range [0.7, 1] is negligible for all the structural materials considered, whereas the variation in mechanical characteristics with temperatures between 20 and 280 K is barely observable only for the case of AA 2219 above 100 K, well away the cryogenic conditions. Such a low sensitivity is mainly due the adoption of a minimum value for the thickness of tank walls, as prescribed by [39].

3.1.2. Sensitivity to Insulation Materials

As completed for the structural materials, the present section shows the effects of varying the material selected for the insulation layer and t_{ins} , considering a tank made of AA2219 with $L/D_{str} = 1.5$, $d_{supp}/L = 0.8$, and $f_{end} = 0.6$. Since insulant density influences the structural sizing, the figure of merit considered here is the empty mass fractions μ_{tank} , defined according to Equation (49), which is the sum of structural and insulant mass fractions. As can be recognised, lower μ_{tank} values are expected to provide better aircraft performance.

$$\mu_{tank} = \frac{M_{str} + M_{ins}}{V_{int} \cdot \rho_{LH}} \tag{49}$$

A range comparison is provided to evaluate the possible effects on aircraft performance; hence, the external tank radius is adapted as t_{ins} varies to keep the same V_{int} value. Results depicted in Figure 17a show that polystyrene foam (PS), given its lower density, performs better in terms of μ_{tank} . Less obvious are the results in terms of flight range given by Figure 17b, which underlines that different insulation foams provide similar range performance, and that this latter improves significantly only up to t_{ins} values around 100 mm. This indicates that, increasing t_{ins} above this value, a balance is reached between the reduction in vented LH₂ and the increase in LH₂ consumption due to the overall weight increase.

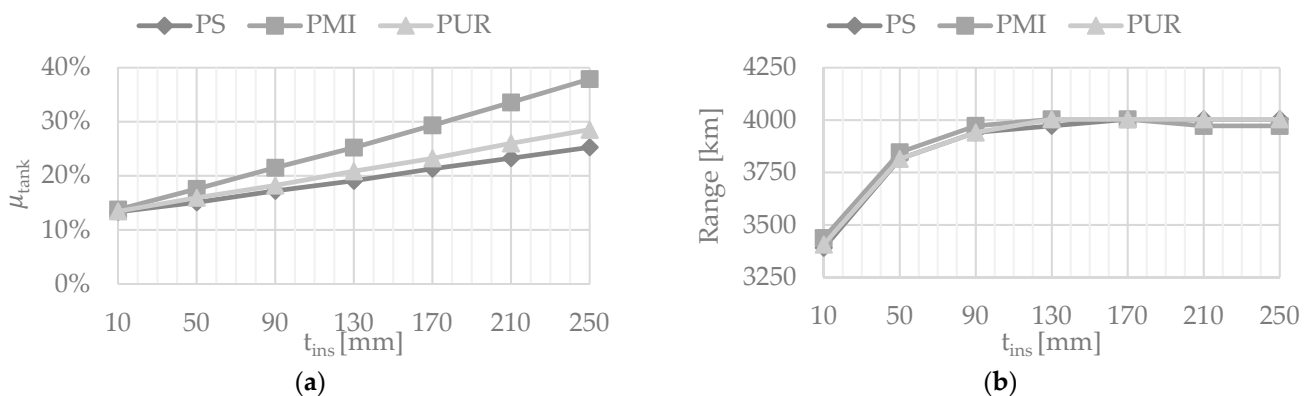
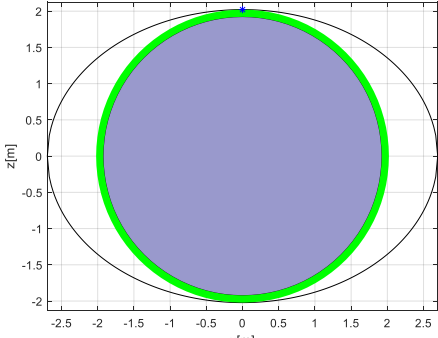


Figure 17. Influence of insulant material selection and layer thickness (t_{ins}) on empty mass fraction μ_{tank} (a) and range flown (b), assuming the same internal volume available for LH₂.

The constant volume assumption has no practical applications, since if t_{ins} is increased, the internal radius (hence V_{int}) has to be reduced to keep the compatibility with the section dimensions. Therefore, the following results refer to the same tank considered in the previous analysis, described in Table 8, in which the maximum available radius refers to the PARSIFAL case (Table 1) and insulant material is the polystyrene foam.

Table 8. Data on the reference single tank/full section configuration.

Parameter	Value	Cross-Section (Example)
Maximum tank radius (R) [m]	2.02	
Tank layout	Full-section	
Number of tanks in the section	1	
N. of tank groups (n_{tg})	1	
R_{min} [m]	0.50	
Catwalk width [m]	Not present	
t_0	90°	
t_{ins} [mm]	Variable	
L/D_{str}	Variable	
D_{str} [m]	Variable	
d_{supp}/L	0.80	
f_{end}	0.60	

The iso-range curves shown in the charts of Figure 18 show that for any value of L/D_{str} , longer ranges are achievable if t_{ins} is close to 50 mm. A possible explanation is that moving from any point of the charts to lower t_{ins} values, the inertial loads due to the insulant are smaller and lead to thinner tank structures. The lower the thickness of these two layers, the larger the internal radius, which allows to embark the same amount of LH₂ with a shorter tank.

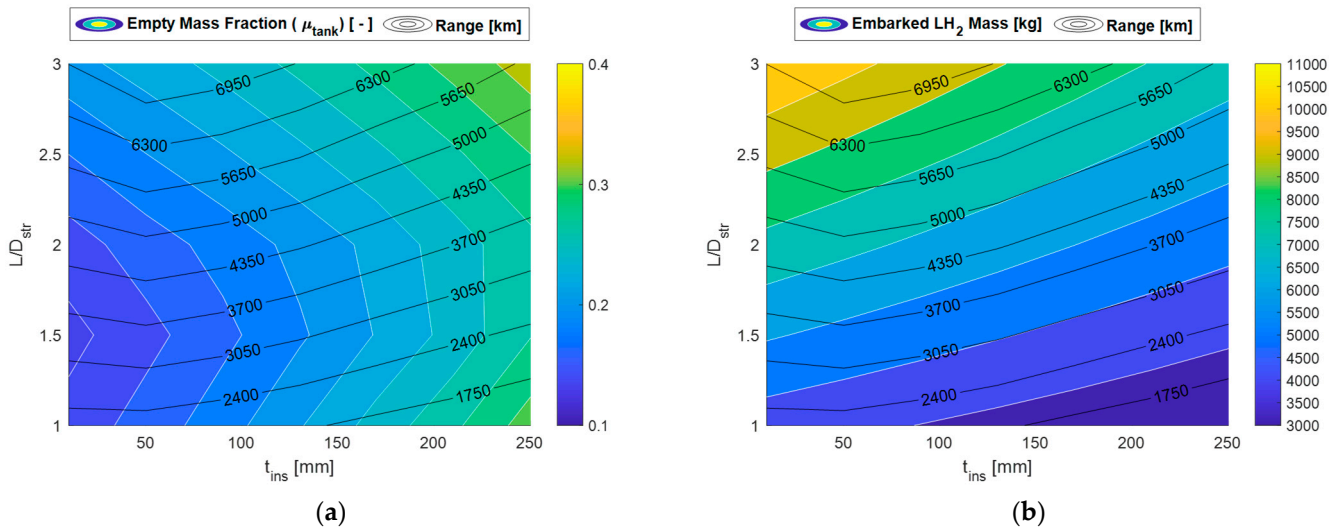


Figure 18. Sensitivity to length-to-diameter ratio (L/D_{str}) and insulant thickness (t_{ins}) with indication of flight range: (a) empty mass fraction (μ_{tank}) and (b) embarked LH₂ mass.

At the same time, reducing t_{ins} increases the heat exchange, hence a larger fraction of LH₂ is vented-out and a longer tank is needed to compensate this loss. These two opposite effects drive the shape of the iso-range curves shown in the following charts, determining an optimal value of t_{ins} , that, for the materials' properties considered here, is around 50 mm. Moreover, this optimality condition is more evident as L/D_{str} increases.

Figure 18a indicates that, for an assigned value of t_{ins} , μ_{tank} reaches the lowest values as L/D_{str} approaches 1.5, which confirms the choices described at the end of Section 3.1.1. From Figure 18b, it is possible to observe that the gradient of iso-LH₂ curves is well-aligned with the gradient of the iso-range curve only for high values of t_{ins} , meaning that as this latter decreases the mass of LH₂ is not useful to extend the flight range, i.e., the vented fraction increases. As already observed in Figure 17b, for $L/D_{str} = 1.5$ this alignment is reached when t_{ins} approaches 100 mm.

3.2. Tanks–Fuselage Integration Studies Based on Full-Section Layouts

3.2.1. Sensitivity to t_0 and t_{ins} under Different Layout Constraints

The results presented in this section were obtained using the data in Table 8, assigning to t_{ins} a variable value and setting as a constant the tube length $L = 5.9$ m (which provides $L/D_{str} = 1.5$ for the main tank, Tank#0). The number of tanks in the section was not fixed a priori and 3 possible conditions were considered: no constraints on the R_{min} value (Figure 19a), $R_{min} = 0.5$ m (Figure 19b), and $R_{min} = 0.5$ m with a 0.8-m-wide catwalk (Figure 19c). Some examples of cross-sections are illustrated in Appendix D, for $t_{ins} = 50$ mm.

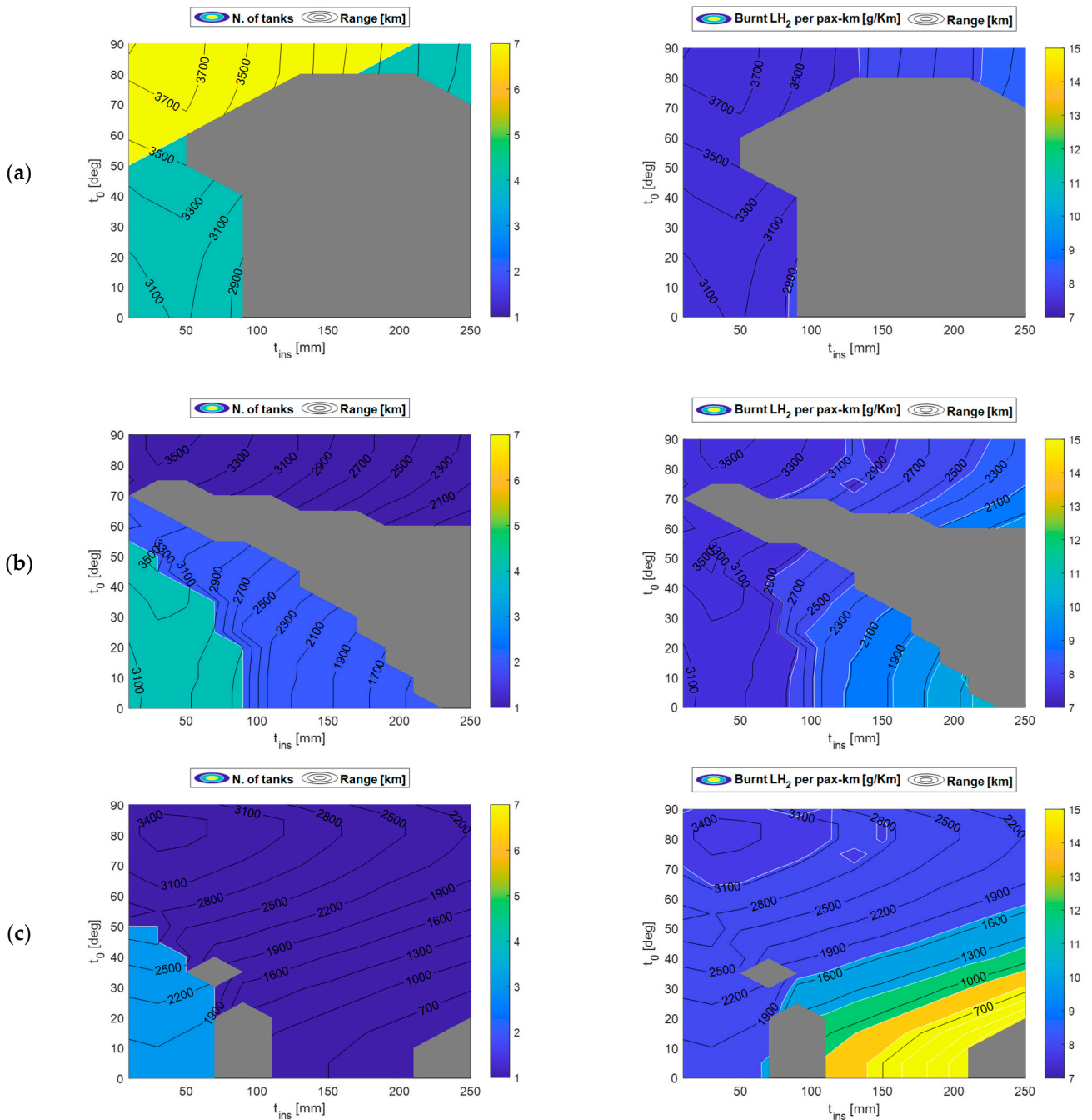


Figure 19. Sensitivity of number of tanks (left) and burnt LH₂ per pax-km (right) to t_0 and t_{ins} , with range indication: (a) without R_{min} constraint; (b) with $R_{min} = 0.5$ m; (c) with $R_{min} = 0.5$ m and catwalk width = 0.8 m.

The grey areas in Figure 19 charts indicate that the $(L/D_{str}, t_{ins})$ pair is not able to fulfil the minimum internal pressure requirement for the whole mission duration; therefore, the solution is indicated as not feasible for safety reasons. A possible countermeasure to this problem would be the implementation of a specific pressure-dependent strategy to control the LH₂ outflow from each tank, whereas in this preliminary study a constant LH₂ flow was considered for all the non-empty tanks.

The main observations concerning the results shown in Figure 19 are:

- The need to define a proper R_{min} value is not only related to manufacturability but derives from thermodynamic reasons too. In fact, too small LH₂ volumes are affected by minimum internal pressure problems which lead to a wide unfeasible region (Figure 19a);
- When the R_{min} constraint is introduced, the solutions which maximise the ranges and minimise LH₂ per pax-km consumption, are in the neighbourhood of $t_0 = 90^\circ$ and $t_{ins} = 50$ mm and are characterised by only 1 tank in the section (Figure 19b). In this case, the seat capacity is 204;
- The introduction of the catwalk breaks the symmetry of the solution, moving the optimum far away from the configuration with $t_0 = 90^\circ$. In the case at hand, the optimal condition is reached for t_0 close to 80° , without any effects on seat capacity.

The LH₂ per pax-km consumption is slightly affected by different number of passengers, which vary because t_{ins} has a weak but not null effect on tanks' total lengths, according to Equation (2). The seat capacity of the previous cases can be increased by 1 row for several $(L/D_{str}, t_{ins})$ combinations, whereas few cases allow to add 2 rows.

3.2.2. Sensitivity to L/D_{str}

The results given in this section were obtained considering the data in Table 9, set as reference for a single tank/full section configuration with a catwalk, and assigning L/D_{str} the role of variable. The case with the catwalk was selected since it does not introduce a physical interruption in the cabin, hence it is more in line with today's regulations.

Table 9. Data on the reference single tank/full section configuration with a catwalk.

Parameter	Value	Cross-Section (Example)
Maximum tank radius (R) [m]	2.02	
Tank layout	Full-section	
Number of tanks in the section	1	
N. of tank groups (n_{tg})	1	
R_{min} [m]	0.50	
Catwalk width [m]	0.80	
t_0	80°	
t_{ins} [mm]	50	
L/D_{str}	Variable	
D_{str} [m]	3.94	
d_{supp}/L	0.80	
f_{end}	0.60	

Figure 20a shows the effects of tank's length on number passengers and range, providing the input to find a trade-off condition.

Although the latter depends on the desired market placement of the aircraft, Figure 20b can support the trade-off study providing relevant information from the environmental impact point of view, such as the consumption per pax-km and the vented LH₂ mass fraction. Figure 20a also shows that if target range is set to equal the harmonic range of the reference aircraft (5722 km, see Table 7), the maximum passenger capacity would be reduced from 308 to 164 units (18 seat rows less). It is worth underlining that the impact of range extension on passenger capacity is actually milder, since for short ranges (<1000 km) there is an initial loss of 56 passengers (7 rows).

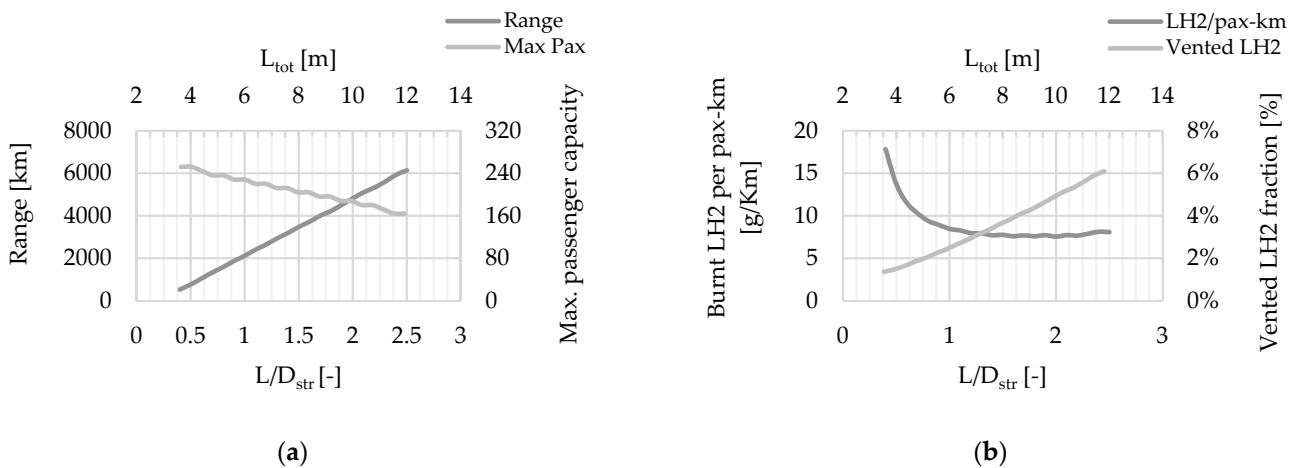


Figure 20. Sensitivity to L/D_{str} : (a) range and seat capacity, (b) burnt LH₂ per pax-km and vented mass fraction.

3.2.3. Multiple Groups of Tanks

To evaluate pros and cons of using multiple groups of tanks, comparisons with the single tank cases given in Table 8 were performed. For each $(L/D_{str}, t_{ins})$ pair, 2 groups of single tanks were derived, under the constraint of keeping the total LH₂ embarked mass unvaried (Equation (16)).

With 2 tanks, the number of endcaps is doubled, hence the fuselage portion that needs to be transformed from the passenger cabin into the tank bay is longer. For the cases at hand, such difference leads to a reduction in 2 or 3 seat rows (16–24 passengers), depending on t_{ins} value, which leads to take-off weight reduction (2%, on average).

Figure 21a shows that the double tank solution exhibits lower μ_{tank} values as t_{ins} decreases, and in most cases, it also reduces the vented hydrogen amount. The weight reduction, as well as the advantages introduced in structural and thermodynamic behaviour, determine an increase in flight range, which as Figure 21b shows, is more significant as t_{ins} is reduced.

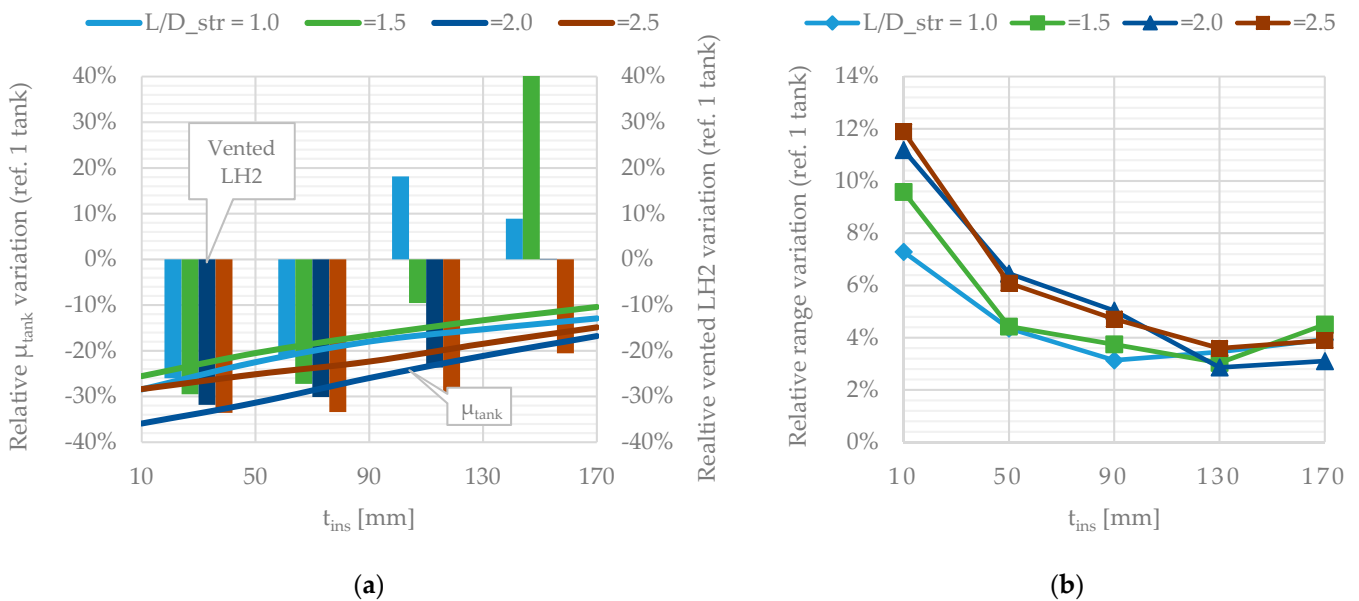


Figure 21. Comparison between 2 tanks and 1 tank configurations with the same embarked LH₂: (a) relative μ_{tank} and vented LH₂ variations, (b) relative range variation (reference values: 1 tank).

By setting $L/D_{str} = 2.5$ and $t_{ins} = 50$ mm, it was observed that, compared to the case of a single group, the range increases of 6% and 10% for 2 and 3 groups of tanks were observed, respectively, whereas there is a penalisation in terms of passenger capacity (−10% and −20% approximatively). It is worth mentioning that a multiple tank solution allows to deal with other aspects not faced in the present work, such as aircraft balancing, stability, and control, with more flexibility.

3.3. Tanks–Fuselage Integration Studies Based on Part-Section Layouts

The part section layout has the advantage of avoiding the reduction in passenger capacity, since tanks can be located under the cabin floor, although this would limit the volume available for freight and checked baggage.

In this section, results of achievable performance refer to the data reported in Table 10, in which 2 tank groups were considered in order to increase the embarked LH₂.

Table 10. Data on the reference multi tank/part-section configuration (cargo deck).

Parameter	Value	Cross-Section (Example)
Maximum tank radius (R) [m]	2.02	
Tank layout	Part-section ($y_L = -0.50$ m)	
Number of tanks in the section	Variable	
N. of tank groups (n_{tg})	2	
R_{min} [m]	0.25	
Catwalk width [m]	Not present	
t_0	−90°	
t_{ins} [mm]	Variable	
L/D_{str}	Variable	
D_{str} [m]	Variable	
d_{supp}/L	0.80	
f_{end}	0.60	

As Figure 22a shows, the maximum range is close to 3800 km which is about 65% of the reference aircraft harmonic range. Such solution, characterised by high aspect-ratio tanks ($L/D_{str} = 2.5$) with thin insulation layers (<50 mm), allows also to reach LH₂ per pax-km consumption values as low as 5 g/pax/km.

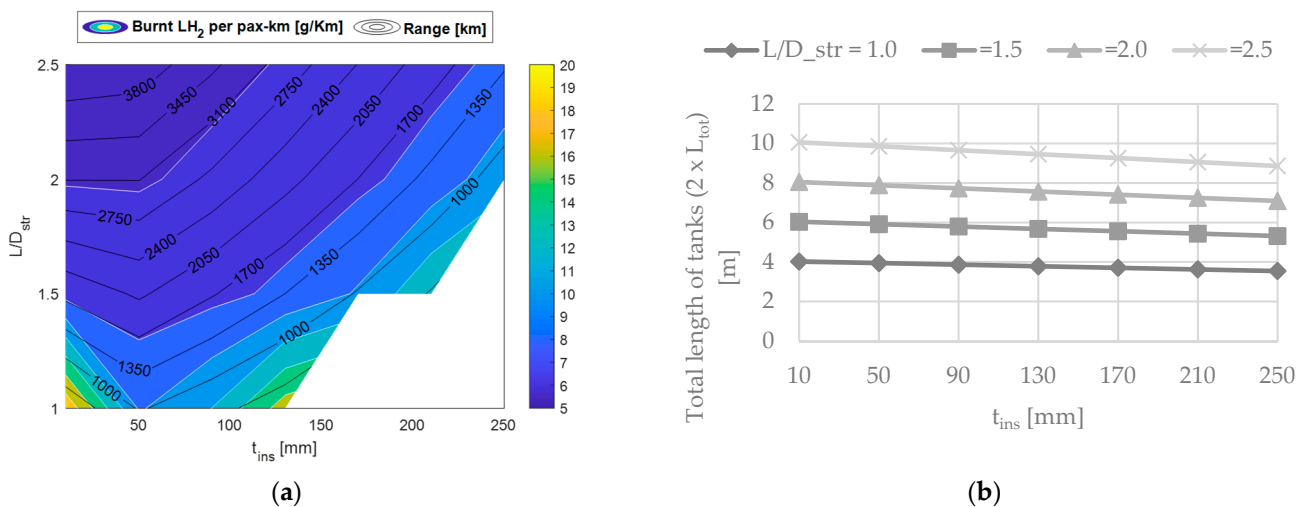


Figure 22. Part-section layout (cargo deck) with 2 groups of tanks: (a) sensitivity of burnt LH₂ per pax-km to L/D_{str} and t_{ins} , (b) total length of tanks (2 groups).

In addition, the total length of both the tanks' groups is close to 10 m (Figure 22b), which appears to be compatible with the fuselage dimensions. The white areas in Figure 22 refer to cases in which the tank volume is not sufficient to complete the mission.

4. Conclusions

The present paper illustrates a parametric approach for the investigation, at conceptual level, of the performance of short-medium-range aircraft with hydrogen propulsion. Aiming at assessing the impact of introducing LH₂ propulsion systems on aircraft performance, a retrofitting approach focused on effect of cryogenic tanks integration in given aircraft geometries was adopted. LH₂ tanks were modelled as non-integral pressure vessels, composed of a central tube and semi-ellipsoidal endcaps, and were sized to fit into the fuselage of a reference aircraft, under the assumption that its main aerodynamic, flight mechanic and structural characteristics were not affected. The chosen reference aircraft for such purpose is a box-wing short-medium-range airplane, resulting from a previous European research project called PARSIFAL, which has been proven to cut the fuel consumption per passenger-kilometre up to 22%, with similar benefits on CO₂ emissions and global warming potential. This is the result of exploiting the superior aerodynamic efficiency of the box-wing systems to design a wider fuselage, increasing the 6-seat abreast of conventional comparable aircraft to 8, while keeping the wingspan within the same limit of 36 m. Therefore, the combination of available internal volume and high aerodynamic performance given by the box-wing architecture represents the scientific foundation of this study, aiming at a first assessment of the operational capacity given by the LH₂ propulsion.

By acting on few geometric parameters, the approach allows to define a wide variety of fuselage-tank cross-section layouts, with the possibility of varying the number, size, and position of tanks. In addition, it is possible to introduce a catwalk constraint, which allows to create a corridor next to the tanks, and to multiply the number of tank groups along the fuselage axis. An assessment workflow was also implemented to perform the structural sizing of the tanks and analyse their thermodynamic behaviour during the mission.

The structural model, based on the ASME Boiler and Pressure Vessel Code, was calibrated by means of FEM analyses mostly devoted to estimating the buckling resistance, since it is the sizing criterion for most of the tanks with a length-to-diameter ratio (L/D_{str}) higher than 1. Sensitivity analyses were performed varying the structural materials, selected among typical metallic alloys used for cryogenic applications, and observing that the lighter material, i.e., the aluminium alloy AA2219, although the lower mechanical characteristics minimise the structural mass fraction of tanks. The structural analyses also provided a set of guidelines to assign a value to geometric parameters such as the endcaps aspect ratio ($f_{end} > 0.4$), length-to-diameter ratio ($L/D_{str} > 1.5$), and non-dimensional distance between supports ($d_{supp}/L < 0.8$).

The LH₂ present in the tank is constantly subject to evaporation and, depending on the internal pressure, it is expelled in gas form; therefore, its depletion depends both on the fuel request and to these venting mechanics, which both have an influence on flight range. Therefore, this latter was estimated by simulating the flight missions with a time-marching approach that couples the fuel request from engines with the thermodynamics of the LH₂ in the tanks, whose surface is completely covered by an insulation layer. Therefore, sensitivity analyses of flight range to insulant material and its thickness were performed, indicating that better performance is achieved using polystyrene foam with thickness around 50 mm. This latter optimal condition is more evident as L/D_{str} increases.

Given such preliminary results concerning the tanks' shape and their technological aspect, the focus of the study was moved towards the possible fuselage-tank cross-section layouts. Part-section layouts, with tanks located under the cabin floor, do not affect passenger capacity and allow to achieve flight ranges up to 4000 km (about 65% of the reference aircraft harmonic range). For longer ranges, a full-section layout, provided with a catwalk corridor for safety reasons, is required. These solutions are designed to maximise the embarked LH₂ in the given fuselage cross section but leads to a reduction in passenger

capacity proportional to tanks' lengths. In fact, in the range interval between 4000 and 6000 km, the number of passengers reduces from 196 to 164, against 308 of the part-section layouts. Figure 23 summarises the most relevant results in terms of transport capabilities, i.e., passenger capacity and harmonic range, compared to the reference aircraft. As shown, aiming at a high passenger capacity goal, a part-section layout is preferable, whereas the full-section layout, with the LH₂ mass stored in more than one group of tanks, is a better solution to cover longer flight ranges. In addition, multiple tanks allow more flexibility in dealing with aircraft balancing, stability, and control, which are not faced in this work and should be part of future investigations. Since each solution is associated to different tanks' lengths, any choice needs to be verified with respect to the actual availability of fuselage volume.

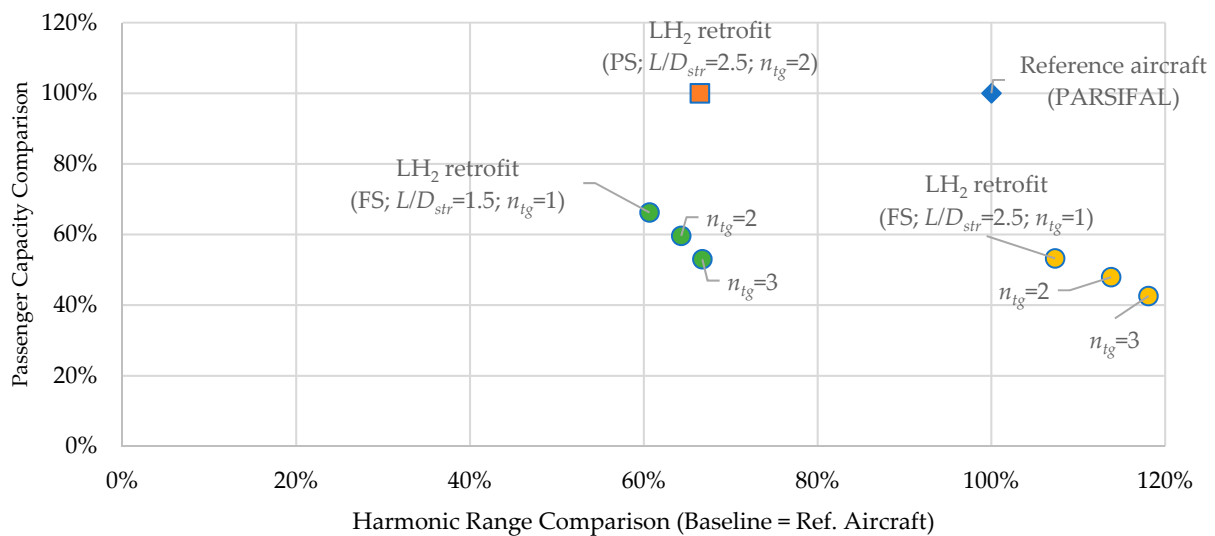


Figure 23. Summary of transport capabilities for some of the investigated LH₂ aircraft configurations compared to the reference aircraft (308 pax, 5722 km), for both part-section (PS) and full-section (FS) integration layouts.

Concerning open problems and possible further development paths for this research, it is worth mentioning the implementation of a flow control strategy, depending on internal pressure and capability of limiting both venting and minimum pressure problems, the integration of constraints about flight mechanics (e.g., effects of longitudinal trim and stability at each time step), the implementation of a thermodynamic model capable of taking the mutual interaction between tank installed in the same fuselage portion into account, as well as more detailed studies about the structural connection between the tanks and the fuselage, with the implementation of a higher fidelity model to estimate the aircraft empty weight.

Author Contributions: Conceptualization, V.C. and D.Z.; Data curation, V.C., D.Z. and V.B.; Formal analysis, V.C., D.Z. and V.B.; Methodology, V.C., D.Z., K.A.S. and V.B.; Software, V.C., D.Z., K.A.S., V.B. and G.P.; Supervision, V.C.; Validation, V.C., D.Z. and V.B.; Visualization, V.C., D.Z. and V.B.; Writing—original draft, V.C., D.Z. and K.A.S.; Writing—review & editing, V.C., D.Z., K.A.S., V.B. and G.P. All authors have read and agreed to the published version of the manuscript.

Funding: This research received no external funding.

Conflicts of Interest: The authors declare no conflict of interest.

Appendix A. Energy Derivative

The term Φ in Equation (25) is the “energy derivative” and is defined in Equation (28), according to [31]. This term is non-dimensional; however, its interpretation is easier if represented with the units of [Pa/(J/m³)]. These units identify the energy derivative as the

pressure rise per unit energy input in a unit volume [25]. It is worth noting that the energy derivative is defined for the homogeneous fluid and not on specific phase quantities, and that is variable during the mission.

The energy derivative relative to a state can be computed starting from Equation (28), considering a closed rigid tank of unit volume, with the same homogeneous fluid pressure P and density ρ (or specific volume v) of the considered state. The computation is completed according to the following the steps:

- In the fluid reference condition (state 1), is possible to determine the quality X (Equation (A1)), deriving it from the properties of the saturated H_2 liquid and gaseous phases [40], since they are directly linked to the current pressure.
- Knowing the quality of the fluid X and the internal energies of each phase (u_g, u_l again directly determined by the current pressure), it is possible to compute the homogeneous fluid's overall internal energy (u) according to Equation (A2).
- Adding an arbitrary pressure increase to the tank, the overall density will not change, since it is a closed system. The pressure increase, however, will change the properties of the liquid and gaseous phases (state 2), leading to a variation in the quality X and internal energy u , which can be computed for the new state, again using Equations (A1) and (A2).
- The part of Equation (28) corresponding to du/dP can be approximated by Equation (A3). du/dP is computed at constant overall density, as required by Equation (28), due to the closed tank assumption.
- Φ can be finally computed by Equation (28) considering the state 1 density

$$X = \frac{v - v_l}{v_g - v_l} \tag{A1}$$

$$u = u_l + X(u_g - u_l) \tag{A2}$$

$$\frac{\Delta u}{\Delta P} = \frac{u_2 - u_1}{P_2 - P_1} \tag{A3}$$

Figure A1 shows the comparison of the estimation of the energy derivative computed with this method with the graphs reported in [31].

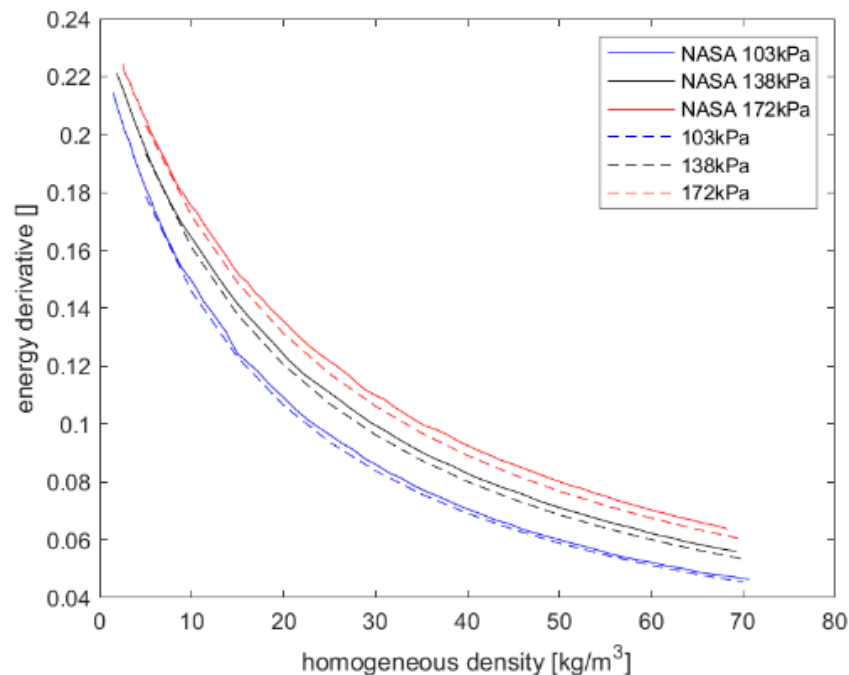


Figure A1. Energy derivative estimation comparison with [31].

Appendix B. Venting Mass Flow Computation

When $P \geq P_{vent}$, the venting valve is activated. The venting valve mass flow (m_{vent}) is considered variable in such way that the pressure inside the tank is kept constant. The computation of m_{vent} is completed imposing $dP/dt = 0$ in Equation (25) as in the following formulas (Equation (A5)).

$$\frac{dP}{dt} = 2 \frac{\Phi}{V} \left[Q - m_o (h_g - h_l) \left(X_o + \frac{\rho_g}{\rho_l - \rho_g} \right) \right] = 0 \tag{A4}$$

$$A = \frac{\rho_g}{\rho_l - \rho_g} \tag{A5}$$

$$m_o (X_o + A) = \frac{Q}{h_g - h_l} \tag{A6}$$

$$(m_v + m_f) \left(\frac{m_v}{m_v + m_f} + A \right) = \frac{Q}{h_g - h_l} \tag{A7}$$

$$\frac{m_v^2}{m_v + m_f} + \frac{m_v m_f}{m_v + m_f} + m_v A + m_f A - \frac{Q}{h_g - h_l} = 0 \tag{A8}$$

$$B = m_f A - \frac{Q}{h_g - h_l} \tag{A9}$$

$$m_v^2 + m_v m_f + m_v^2 A + m_v m_f A + m_v B + m_f B = 0 \tag{A10}$$

Since m_f is known from the mission analysis, Equation (A10) is a second-grade equation in the venting mass flow m_v , which can be solved with the standard second-grade equations solution formula. The solution gives two values of m_v , generally one positive and one negative, the correct solution to take is the positive one.

Appendix C. Liquid Hydrogen Thermal Expansion Coefficient Computation

The LH₂ volumetric thermal expansion coefficient knowledge is necessary to estimate the natural convection inside the liquid phase of the saturated H₂. Unfortunately, this characteristic is not present in the H₂ properties database [36]; however, it is possible to derive it from other properties. The volumetric thermal expansion coefficient β is defined as follows:

$$V_2 = V_1 + \Delta V = V_1 (1 + \beta \Delta T) \tag{A11}$$

where V_1 and V_2 are the substance volumes before and after a temperature change and $\Delta T = T_2 - T_1$ is the difference between the final temperature and the initial one. Equation (A11) could be rearranged as in Equation (A12), considering that temperature increase is acting on the same unit mass of fluid ($M = \rho_1 V_1 = \rho_2 V_2$).

$$\beta = \frac{1}{\Delta T} \left(\frac{V_2}{V_1} - 1 \right) = \frac{1}{\Delta T} \left(\frac{\rho_1}{\rho_2} - 1 \right) \tag{A12}$$

By applying Equation (A12) between two arbitrary temperatures, it is possible to determine the volumetric thermal expansion coefficient of the saturated LH₂, since the density data are known from [36].

Appendix D. Fuselage–Tank Sections of the Full Section Layout Configurations

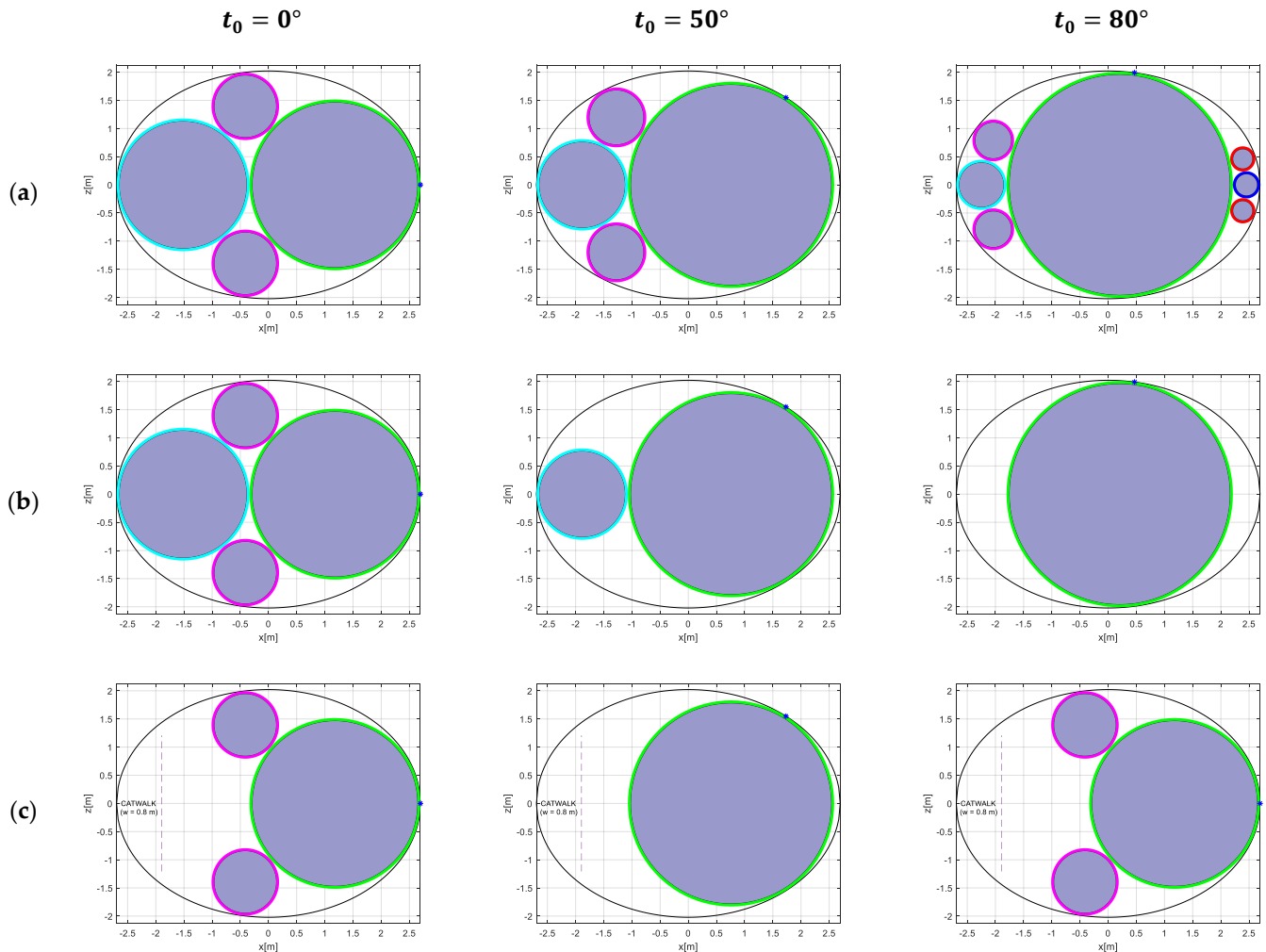


Figure A2. Fuselage and tank cross-sections: (a) without R_{min} constraint; (b) with $R_{min} = 0.5$ m; (c) with $R_{min} = 0.5$ m and catwalk width = 0.8 m.

References

1. ACARE (Advisory Council for Aviation Research and Innovation in Europe). *Strategic Research and Innovation Agenda (SRIA)*; ACARE: Brussels, Belgium, 2017; Volume 1.
2. European Commission. *Flightpath 2050: Europe's Vision for Aviation*. European Commission, Directorate General for Research and Innovation, Directorate General for Mobility and Transport; European Commission: Brussels, Belgium, 2011.
3. Thomson, R.; Weichenhain, U.; Sachdeva, N.; Kaufmann, M. *Hydrogen: A Future Fuel for Aviation?* Roland Berger GmbH: Munich, Germany, 2020.
4. *Clean Sky 2 JU and FCH 2 JU Report. Hydrogen-Powered Aviation: A Fact-Based Study of Hydrogen Technology, Economics, and Climate Impact by 2050*; McKinsey & Company for European Commission: Brussels, Belgium, 2020.
5. Verstraete, D.; Hendrick, P.; Pilidis, P.; Ramsden, K. Hydrogen fuel tanks for subsonic transport aircraft. *Int. J. Hydrogen Energy* **2010**, *35*, 11085–11098. [[CrossRef](#)]
6. PARSIFAL Project: "Prandtlplane ARchitecture for the Sustainable Improvement of Future AirLanes". EU Horizon 2020, 2017–2020 (GA. 723149). Available online: <https://perma.cc/5ULW-HCP4> (accessed on 1 July 2022).
7. Abu Salem, K.; Binante, V.; Cipolla, V.; Maganzi, M. PARSIFAL project: A breakthrough innovation in air transport. *Aerotec. Missili Spaz.* **2018**, *97*, 40–46. [[CrossRef](#)]
8. Cipolla, V.; Frediani, A.; Abu Salem, K.; Picchi Scardaoni, M.; Nuti, A.; Binante, V. Conceptual design of a box-wing aircraft for the air transport of the future. In Proceedings of the AIAA Aviation Forum, 2018 Aviation Technology, Integration, and Operations Conference, Atlanta, GA, USA, 25–29 June 2018. [[CrossRef](#)]
9. Cipolla, V.; Abu Salem, K.; Picchi Scardaoni, M.; Binante, V. Preliminary design and performance analysis of a box-wing transport aircraft. In Proceedings of the AIAA SciTech 2020 Forum, Orlando, FL, USA, 6–10 January 2020. [[CrossRef](#)]

10. Tasca, A.L.; Cipolla, V.; Abu Salem, K.; Puccini, M. Innovative box-wing aircraft: Emissions and climate change. *Sustainability* **2021**, *13*, 3282. [[CrossRef](#)]
11. Prandtl, L. *NACA-TN-182. Induced Drag of Multiplanes*; NACA: Cleveland, OH, USA, 1924.
12. Carini, M.; Méheut, M.; Kanellopoulos, S.; Cipolla, V.; Abu Salem, K. Aerodynamic analysis and optimization of a boxwing architecture for commercial airplanes. In Proceedings of the AIAA SciTech 2020 Forum, Orlando, FL, USA, 6–10 January 2020. [[CrossRef](#)]
13. NASA Project Bee (B57-B). 1965. Available online: <https://www.grc.nasa.gov/WWW/portal/apps/naca/> (accessed on 1 July 2022).
14. Reynolds, T.W. *NACA-RM-E56K08a. Experimental Study of Foam-Insulated Liquefied-Gas Tanks*; NACA: Cleveland, OH, USA, 1957.
15. Fleming, W.A. *NACA-RM-E56E14. Turbojet Performance and Operation at High Altitudes with Hydrogen and JP4*; NACA: Cleveland, OH, USA, 1956.
16. Reynolds, T.W. *NACA-RM-E55F22. Aircraft-Fuel-Tank Design for Liquid Hydrogen*; NACA: Cleveland, OH, USA, 1955.
17. Silverstein, A. *NACA-RM-E55C28a. Liquid Hydrogen as a Jet Fuel for High-Altitude Aircraft*; NACA: Cleveland, OH, USA, 1955.
18. Berry, W. *NASA-CR-112204. A Fuel Conservation Study for Transport Aircraft Utilizing Advanced Technology and Hydrogen Fuel*; NASA: Hampton, VA, USA, 1972.
19. Brewer, G.D. *NASA-CR-132559. Study of the Application of Hydrogen Fuel to Long Range Subsonic Transport Aircraft*; NASA: Burbank, CA, USA, 1975; Volume 2.
20. Snow, D.B. *NASA-TM-X-71994. A Study of Subsonic Transport Aircraft Configurations Using H₂ and CH₄*; NASA: Hampton, VA, USA, 1974.
21. Brewer, G.D. *NASA CR-2700. LH2 Airport Requirements Study*; NASA: Burbank, CA, USA, 1976.
22. *CRYOPLANE-Liquid Hydrogen Fuelled Aircraft—System Analysis. Final Technical Report (Published Version), Contract G4RD-CT-2000-00192. Project GRD1-1999-10014*; Airbus Deutschland GmbH: Hamburg, Germany, 2003.
23. Sippel, M.; Kropp, A.; Mattson, D.; Freund, J.; Tapeinos, I.; Koussios, S. Final Results of Advanced Cryo-Tanks Research Project CHATT. In Proceedings of the 6th EUCASS Conference, Krakau, Poland, 29 June–3 July 2015.
24. Winnefeld, C.; Kadyk, T.; Bensmann, B.; Krewer, U.; Hanke-Rauschenbach, R. Modelling and Designing Cryogenic Hydrogen Tanks for Future Aircraft Applications. *Energies* **2018**, *11*, 105. [[CrossRef](#)]
25. Verstraete, D. The Potential of Liquid Hydrogen for Long Range Aircraft Propulsion. Ph.D. Thesis, Cranfield University, Cranfield, UK, 2009.
26. Brewer, G.D. *Hydrogen Aircraft Technology*; CRC Press: London, UK, 1991.
27. Corchero, G.; Montanes, L. An approach to the use of hydrogen for commercial aircraft engines. *J. Aerosp. Eng.* **2005**, *219*, 35–44. [[CrossRef](#)]
28. NACA. *NACA-RM-E57D23. Hydrogen for Turbojet and Ramjet Powered Flight*; NACA: Cleveland, OH, USA, 1957.
29. Gomez, A.; Smith, H. Liquid hydrogen fuel tanks for commercial aviation: Structural sizing and stress analysis. *Aerospace Sci. Technol.* **2019**, *95*, 105438. [[CrossRef](#)]
30. Prewitz, M.; Bardenhagen, A.; Beck, R. Hydrogen as the fuel of the future in aircrafts—challenges and opportunities. *Int. J. Hydrogen Energy* **2020**, *45*, 25378–25385. [[CrossRef](#)]
31. Lin, C.S. *NASA-TM-104409. A Pressure Control Analysis of Cryogenic Storage Systems*; NACA: Cleveland, OH, USA, 1991.
32. Mital, S.K. *NASA-TM-2006-214346. Review of Current State of the Art and Key Design Issues with Potential Solutions for Liquid Hydrogen Cryogenic Storage Tank Structures for Aircraft Applications*; NACA: Cleveland, OH, USA, 2006.
33. Verfondern, K.; Cirrone, D.; Molkov, V.; Makarov, D.; Coldrick, S.; Ren, Z.; Wen, J.; Proust, C.; Friedrich, A.; Jordan, T. *Handbook of Hydrogen Safety. Chapter on LH2 safety (Project PRESLHY)*; Karlsruher Institut fuer Technologie: Karlsruhe, Germany, 2021.
34. Kuhn, M. *Storage Density of Hydrogen*; Institute of Air Handling and Refrigeration (ILK): Dresden, Germany, 2015. Available online: https://commons.wikimedia.org/wiki/File:Storage_Density_of_Hydrogen.jpg (accessed on 1 July 2022).
35. Arnold, S.S.; Bednarczyk, B.A.; Collier, C.S.; Yarrington, P.W. Spherical Cryogenic Hydrogen Tank preliminary Design Trade Studies, AIAA 2007-2290. In Proceedings of the 48th AIAA/ASME/ASCE/AHS/ASC Structures, Structural Dynamics, and Materials Conference, Honolulu, HI, USA, 23–26 April 2007.
36. National Institute of Standards and Technology. *Thermophysical Properties of Fluid Systems*; National Institute of Standards and Technology: Boulder, CO, USA, 2007. Available online: <http://webbook.nist.gov/chemistry/fluid/> (accessed on 1 July 2022).
37. Schwartzberg, F.R.; Osgood, S.H.; Keys, R.D.; Kiefer, T.F. *Cryogenic Materials Data Handbook*; PB 171809; AFRL: Patterson Air Force Base: Dayton, OH, USA, 1966.
38. *ASME Boiler and Pressure Vessel Code, Rules for Construction of Pressure Vessels. Section VIII, Division 1*; American Society of Mechanical Engineers: New York, NY, USA, 2017.
39. *ASME Boiler and Pressure Vessel Code, Rules for Construction of Pressure Vessels (Alternative Rules). Section VIII, Division 2*; American Society of Mechanical Engineers: New York, NY, USA, 2017.
40. Federal Aviation Regulation, Title 14, Chapter I, Subchapter C, PART 25. Airworthiness Standards: Transport Category Airplanes. Available online: <https://www.ecfr.gov/current/title-14/chapter-I/subchapter-C/part-25> (accessed on 1 July 2022).
41. Rohsenow, W.M.; Hartnett, J.R.; Young, I.C. *Handbook of Heat Transfer*, 3rd ed.; McGraw-Hill: New York, NY, USA, 1998.
42. Lienhard, J.H., IV; Lienhard, J.H., V. *A Heat Transfer Textbook*, 3rd ed.; Phlogiston Press: Cambridge, MA, USA, 2008.

43. Abu Salem, K. Development of Design Tools and Methods for Box-Wing Airplanes and Application of the PrandtlPlane Concept to a Short-Medium Range Aircraft. Ph.D. Thesis, University of Pisa, Pisa, Italy, 2021. Available online: <https://etd.adm.unipi.it/> (accessed on 1 July 2022).
44. International Civil Aviation Organization. *Aerodromes: Volume I—Aerodrome Design and Operations. International Standards and Recommended Practices*; ICAO Annex 14: Montréal, QC, Canada, 2009.
45. Abu Salem, K.; Cipolla, V.; Palaia, G.; Binante, V.; Zanetti, D. A physics-based multidisciplinary approach for the preliminary design and performance analysis of a medium range aircraft with box-wing architecture. *Aerospace* **2021**, *8*, 292. [CrossRef]
46. Beltramo, M.; Trapp, D.L.; Kimoto, B.W.; Marsh, D.P. *NASA CR151970. Parametric Study of Transport Aircraft Systems Cost and Weight*; NASA: Moffett Field, CA USA, 1977.
47. Cipolla, V.; Abu Salem, K.; Palaia, G.; Binante, V.; Zanetti, D. A DoE-based approach for the implementation of structural surrogate models in the early stage design of box-wing aircraft. *Aerosp. Sci. Technol.* **2021**, *117*, 106968. [CrossRef]
48. International Civil Aviation Organization. ICAO Aircraft Engine Emissions Databank. 2019. Available online: <https://www.easa.europa.eu/easa-and-you/environment/icao-aircraft-engine-emissions-databank> (accessed on 1 July 2022).
49. Airbus. *Getting to Grips with Aircraft Performance*; Airbus SAS: Leiden, The Netherlands, 2002. Available online: <https://perma.cc/FQ9P-FET4> (accessed on 1 July 2022).